

## Chapter 6

# Pixel and Electronic Crosstalk

In an ideal imager, each pixel is an independent photon detector. Whether current *from the pixel* or charge *in the pixel* is measured, the electrical content and activity in one pixel does not affect its neighbors (or any other pixels across the detector) and vice versa. In a real detector, this is not the case. Electrical signals couple to one another through direct means such as charge spilling from one pixel to its neighbor or indirectly through capacitance or inductance between current carrying buses.

In the case of hybrid CMOS detectors, there is *crosstalk* between neighboring pixels during charge collection, storage, and possibly readout. This is referred to as *pixel crosstalk*. There is also coupling of the signals from pixels that are readout simultaneously through separate channels on the detector and direct coupling between detector bias currents or voltages and pixel signals. These effects are referred to as *electrical crosstalk*. Both pixel and electrical crosstalk will be discussed in the following sections.

### 6.1 Pixel Crosstalk

During charge collection, electrons and holes in the detector bulk can diffuse laterally into neighboring pixels before they arrive at a pixel well. After collection, when the charge is stored in the collecting node, capacitive coupling between neighboring nodes will result in additional crosstalk. We report here on a further coupling mechanism in which charge carriers appear to be moving between pixels. Because the charge is actually being transferred from one pixel to another, we refer to this as **Interpixel Charge Transfer** or **IPCT**. In this chapter we begin by giving a basic overview of these different crosstalk mechanisms. We then present data from cosmic ray events, Fe<sup>55</sup> measurements, and single pixel reset tests that illustrate how pixel crosstalk manifests itself in HyViSI detectors.

### 6.1.1 Mechanisms of Pixel Crosstalk

The term pixel crosstalk applies to a number of separate phenomena that may be occurring in the detector or ROIC simultaneously. Crosstalk can occur between the time photocharges are generated and stored since carriers generated directly above a pixel location can diffuse to neighboring pixels. It can also occur after the charge has been collected via capacitive coupling of neighboring pixels, direct charge transfer through a conductive channel, or thermionic diffusion of carriers over an interpixel potential barrier. The last of these occurs only under rare circumstances and will be saved for discussion until Section 6.1.4.3, where it is relevant. The other forms of crosstalk will be briefly summarized here as a basis for understanding the experimental results that follow.

#### 6.1.1.1 Lateral Charge Diffusion in HyViSI Bulk

After an electron-hole pair is generated in the bulk of the HyViSI, the hole must travel to the collection node before it is counted as signal charge. On its way, it will undergo some lateral diffusion in the bulk material. If there is both an undepleted and depleted region in the bulk or if the detector layer is sufficiently thick, predicting where, on average, the hole will end up is a complicated problem. Pavlov et al. [106] treat this problem in great detail for the case of x-rays in thick CCD detectors, and many of the results are applicable for a SiPIN diode detector. If the detector is an overdepleted state, as the HyViSI should be for astronomical applications, the problem becomes much simpler. O'Connor et al. [107] provide the following expression for the mean diffusion radius of the holes at the collecting surface by assuming the bulk is high resistivity ( $\rho > 10,000\Omega\text{-cm}$ ) and overdepleted:

$$\sigma_D = d \sqrt{\frac{2kT}{qV}}, \quad (6.1)$$

where  $d$  is the detector thickness,  $k$  is Boltzmann's constant,  $T$  is the temperature,  $q$  is the electron charge, and  $V$  is the bias voltage across the detector. While this expression is the result of a simplified treatment, it reveals the two primary "knobs" we can use to reduce the charge diffusion: the detector temperature and the backside voltage  $V_{SUB}$ . Minimizing the lateral diffusion is essential for reducing the PSF to levels suitable for astronomy.

#### 6.1.1.2 Interpixel Capacitance (IPC)

It has been suggested by Moore et al. [24] that interpixel capacitance plays the primary role in coupling the voltages on neighboring pixels in SiPIN detectors. In this model, a pixel at  $i, j$  is described as a capacitor  $C[i, j]$  that receives a signal  $Q[i, j]$  that corresponds to the photocurrent entering the pixel. The detector is modeled as a discrete linear shift-invariant (LSI) system that outputs an array of voltages

$$V[i, j] = Q[i, j] * h_c[i, j], \quad (6.2)$$

where  $*$  is the 2-d discrete convolution operator and  $h_c[i, j]$  is the impulse response of the collection array. Ideally,  $h_c[i, j] = \delta[i, j]/C_{node}$ , since the discrete delta function represents no coupling between neighbors. However, in this model there are coupling capacitors between pixels so that  $h_c[i, j]$  has contributions from neighbors, i.e. pixels with  $i \pm 1$  and  $j \pm 1$ .

The level of coupling is usually measured with the parameter  $\alpha$ , which is the fraction of charge that appears in a neighboring pixel due to IPC. For instance, if only symmetric coupling to the four nearest neighbors is considered, the center pixel loses  $4\alpha$  of its charge and  $\alpha$  of that charge will be measured in any one of the four neighbors. For the asymmetric coupling that is always observed in HxRG detectors, each neighbor will have a unique value  $\alpha_{i,j}$ .

Interpixel capacitance could potentially occur in the ROIC or the detector substrate, or even between these two layers at the level of the indium bump bonds. There is very strong evidence that it does not take place in the ROIC, though. If the coupling took place in the ROIC, we would expect to see the effect between science pixels at the edge of the detector and the neighboring reference pixels. However, in all cases: cosmic ray hits, hot pixel volcanos, single pixel reset experiments, etc., we do not see the reference pixel signal affected by the signal on the neighboring science pixels. We are therefore forced to conclude that the coupling occurs in the bulk of the detector or between the ROIC and detector layer.

The coupling in the IPC model adequately describes the degradation in modulation transfer and point spread functions of the detector. These, in turn, result in an overestimation of the QE of the detector. However, in this model it is assumed that  $h[i, j] \geq 0$ . Physically, this means that charge entering a given pixel does not leave the pixel or get destroyed through recombination. A different mechanism is thus needed to describe the observed behavior in the HyViSI devices, where charge appears to be leave and enter pixels.

### 6.1.1.3 Interpixel Charge Transfer (IPCT)

IPCT manifests itself in the HyViSI detectors in a number of situations. The place where it shows up most strongly is in cosmic ray hits. After the initial spike in signal attributed to a deposit of charge by the cosmic ray, we see a decay in the signal of the central pixels and a rise in the signal of one or more of their neighbors. It also shows up in  $\text{Fe}^{55}$  gain tests, where we see the pixels hit by an x-ray gain and lose signal in a similar fashion.

The precise details of how IPCT occurs are not yet known, in part because we do not know the relevant details of the detector (e.g. the pixel doping, passivant thickness, etc.). However, our initial speculation that it arises at the surface interface between the  $\text{SiO}_2$  passivant and the lightly doped bulk appears to be right. In the latest of the HyViSI sensors we tested—one for which this surface interface was treated differently—the IPCT was dramatically reduced. Nevertheless, in the following sections we will present the empirical results that show the signature of IPCT as it appears in the majority of the devices we tested.

### 6.1.2 Measurement via Cosmic Rays

A striking example of Interpixel Charge Transfer is seen when “cosmic rays” make their way into the detector. The term “cosmic rays” is put in quotes because, as Groom points out [108], in ground based detector systems many of these events are generated by particles that do not have a cosmic origin. The genuine cosmic rays consist primarily of relativistic muons produced by secondary meson decay, and at higher elevation, small fraction of protons, helium nuclei, electrons, positrons, and photons [109]. The other, non-cosmic events are attributed to local sources on the ground such as gamma rays from radioactive decay or beta particles. Smith et al. [110] show evidence that Compton recoil electrons from gamma rays passing through fully depleted CCDs are the primary source of events that deviate from a straight “muon track” or a “spot” generated by a normally incident particle. To validate this, we have performed simulations with the GEANT4 particle physics simulation package. The simulations not only show that Compton recoil electrons indeed give rise to “worm” tracks in thick silicon detectors, but that impact ionization from electrons liberated by a muon passing through the detector can cause secondary tracks (“Delta Rays”) or large spots at random locations along the straight track. The variety of event types seen in the simulations matches well to the data collected with the HyViSI detectors.

While the physical interactions that comprise the cosmic ray events differ greatly, they all share one thing in common: they take place on a timescale ( $t_{event} \sim 10^{-9}$  s) far shorter than the frame time of the detector, even for the case where a very small window of pixels is being read out ( $t_{frame} \sim 10^{-3}$  s).<sup>1</sup> Thus, the expected signature of one of these events should be a large step in signal vs. time for each affected pixel at the read  $r$  following the time when the event took place. After the step, assuming the collecting well is not full, the node should continue to collect photo or dark carriers at the same rate it did before the particle passed through the detector. This sort of behavior, shown in the upper left signal vs. time plot of Figure 6.1, is observed in cosmic ray hits that occur during dark and illuminated exposures at temperatures at or below about 130 K.

At temperatures above 130K, however, the HyViSI detectors quickly depart from this ideal behavior. The other plots in Figure 6.1 show that for these temperatures, the signal decreases after the cosmic ray has passed through the detector. For reasons that will be made clear later in this chapter, it is assumed that the decrease in signal is due to a net charge loss in the pixel. As can be seen in the figure, the total charge lost in a given period of time,  $Q_{lost}$ , increases with increasing temperature while the time it takes for the loss decreases. This behavior begins to change around 180 K. At this point it appears the dark current overrides the charge loss and causes the pixel to begin integrating holes more quickly. While the plots in Figure 6.1 show the behavior at  $V_{SUB} = 5$  V, the charge loss occurs at all voltages tested, all the way up to 40V. There are some subtle effects

---

<sup>1</sup>The incident particles are traveling through the silicon at relativistic speeds, so the event time should be dominated by the time it takes for liberated holes to drift to the integrating node,  $t_{col}$ . Assuming an average electric field of  $E = 10^3$  V/cm and hole mobility of  $\mu_p = 10^4$  cm<sup>2</sup>/s/V in the high purity silicon,  $t_{col} = 1$  ns for a hole that starts at rest and has to traverse the entire depletion region (100  $\mu$ m).

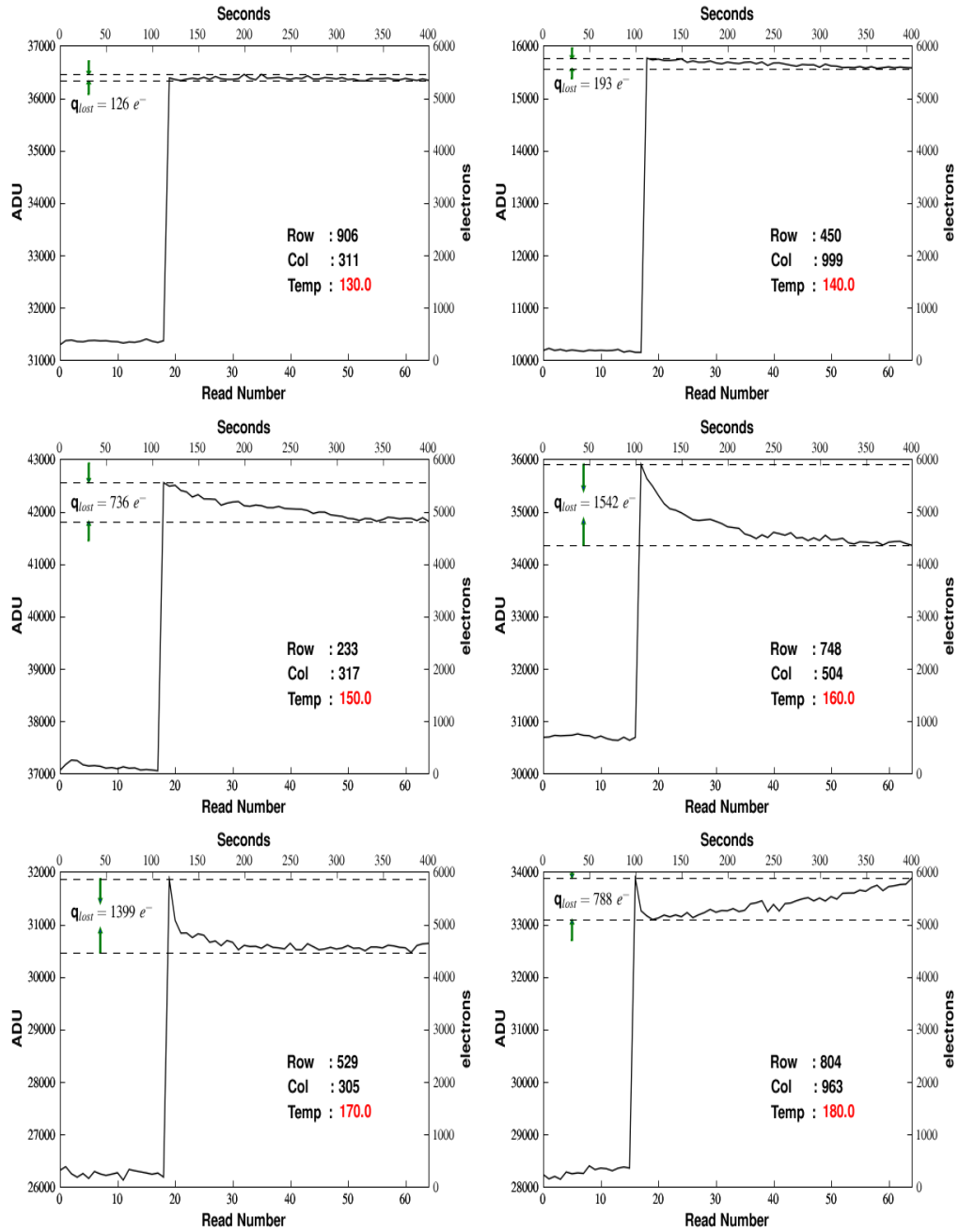


Figure 6.1: Cosmic ray events in H1RG-022 found in 400 second dark exposures at temperatures from 130-180 K and a backside voltage of  $V_{SUB} = 5$  V. The plots show the signal as a function of time in up the ramp integrations. The right-hand scale of the y-axes runs from 0-6000  $e^-$  for all plots. A substantial charge loss,  $q_{lost}$  in the pixels is clearly evident at 150 K and even at 180 K where the dark current is high.

for voltages where the detector is not fully depleted, and these will be discussed in a later section. In this section, the focus will be on the temperature dependence, which is the most dominant factor.

In the range of 130-180 K, the decay of signal after the cosmic ray hit displays an exponential behavior. The rate of decay is proportional to the amount of charge the pixel has yet to lose before the total loss reaches the value  $Q_{lost}$ . In other words, if the pixel has lost the equivalent of  $q_{lost}$  holes at time  $t$  after the cosmic ray hit and will eventually lose  $Q_{lost}$  holes before it starts to integrate positive signal again, then the rate of hole loss can be expressed as

$$\frac{dQ(t)}{dt} \propto -(Q_{lost} - q_{lost}). \quad (6.3)$$

As stated earlier, the constant of proportionality clearly depends on temperature. However, there is some evidence that at a given temperature the constant of proportionality is not actually a constant, but rather depends on the conditions in the neighboring pixels as well as the physical location of interaction in the detector. While important for determining the mechanism that causes the charge loss, this deviation will be ignored and treated as a second order effect for the moment. To first order, if a time constant of  $e_n$  is chosen, then the charge lost in a time  $t$  after the cosmic ray hit will be

$$q_{lost}(t) = Q_{lost}(1 - e^{-e_n t}), \quad (6.4)$$

and the charge measured in a read of the detector,  $Q_{meas}$ , at time  $t$  will be given by:

$$Q_{meas}(t) = Q_{dep}(t = 0) - Q_{lost}(1 - e^{-e_n t}), \quad (6.5)$$

where  $Q_{dep}(t = 0)$  is the number of holes initially deposited in the pixel. Note that because each pixel is sampled at a fixed interval,  $Q_{meas} = Q_{dep}$  only if the cosmic ray interacts immediately before the pixel is read. In all other cases the first measurement of the pixel will yield a result  $Q_{meas} < Q_{dep}$ , and the charge deposit will be underestimated. The impact this has on x-ray energy measurement will be considered in the next section.

At a given temperature, there is also a near-linear relationship between the amount of charge deposited in the pixel and the amount of charge it loses, i.e.

$$Q_{lost} \propto Q_{dep} \quad (6.6)$$

Like the time constant, the deviation from linearity appears to be dependent on conditions in the neighboring pixels. It also depends on the depth at which the charge carriers were generated, as evidenced by long muon tracks in exposures where the detector bulk is not fully depleted. For the vast majority of decays, it is observed that

$$Q_{lost} < m(T) \cdot Q_{dep}, \quad (6.7)$$

where  $m(T)$  is a temperature dependent slope that places an upper bound on the amount of charge the pixel will lose before it starts to integrate once again.

It is important to note that this effect is not particular to any one detector tested. **The charge loss is clearly observable in H1RG-018, H1RG-022, H2RG-001, H2RG-32-147, and H4RG-10-007.** In an attempt to reduce the effect in recent designs—and also for the purposes of reducing the magnitude of IPC in HyViSIs—a different surface treatment was applied to improve the Si-SiO<sub>2</sub> interface at the front surface of the detector (Bai, private communication). In H2RG-148, which is the most recently fabricated detector that we tested, the effect is significantly reduced.

### 6.1.2.1 Description of Cosmic Ray Experiment and Analysis

To measure the amount of charge lost, cosmic ray events were characterized from a large set of 1060 second up the ramp dark integrations obtained with H2RG-001. The exposures each consisted of 100 reads and were taken in 4 output mode, yielding a frame time of  $t_{frame} = 10.6$  s. They were recorded at temperatures from 100 K to 180 K at 10 K intervals. Once all temperatures were probed, the bias voltage was adjusted so that data was recorded at  $V_{SUB} = 5, 10, \text{ and } 15$  volts. Ample time was given for the detector to settle whenever the temperature or  $V_{SUB}$  was adjusted.

Detection of the events is done with a robust method that uses both the temporal information contained in the time axis of the datacube and the two dimensional spatial information in each frame. First, a median dark is formed for each temperature to be used for subtraction of the average dark current in each exposure. For a given exposure, starting at the lower left hand pixel of the array, the pixels ramps are sequentially fitted with a line as discussed in Section 5.2.4. If a discontinuity in the line above a certain threshold is detected, it is flagged as a cosmic ray. For the surrounding pixels that have not yet been evaluated, the difference in signal from the read before,  $r$ , and after,  $r + 1$ , the hit are taken. This difference is referred to as *the step*. If the step is greater than  $3\sigma_{rn}$ , then that pixel is added to the event and the search is continued with its nearest neighbors. After a pixel has been flagged or slope fitted, it is masked with a zero so that it is not counted as part of an event found later in the array.

Once all of the contiguous pixels with a difference of  $3\sigma_{rn}$  have been evaluated for a given event, the entire collection is categorized by global parameters such as its morphology (similar to the methodology described in Groom [108], we classify them as straight muon track, worm, isolated spot, Gaussian spot, delta rays, and unclassified), its minima and maxima in signal increase, etc. Then, for each pixel in the event, the step in signal from  $r$  to  $r + 1$  is recorded as  $Q_{dep}$ , and the decay after the step is analyzed to find a minimum and maximum value. After a clear minimum has been found,  $Q_{lost}$  is recorded as the difference in signal between the step and the minimum after the step, and the decay is fit with Equation 6.4 to yield an estimate of  $e_n$ . All of the recorded values for the individual pixels and the global event are then recorded to a database and the search proceeds to look for the next event.

### 6.1.2.2 Characterization of Decays

The results of the charge decay characterization are conveyed in Figures 6.2 and 6.3. The events in the scatter plot of Figure 6.2 are ones that occurred between 200 and 500 seconds after the start of the integration and had a minimum  $Q_{dep}$  of  $500 e^-$ . The range was chosen so that a good estimate of the slope both before and after the cosmic ray hit can be obtained, and to allow significant decay in signal for the lower temperature range. At each temperature, a line with slope  $m(T)$  and intercept of  $b = 0$  (the charge lost for zero charge deposited must necessarily be zero) is fit to the points to indicate the proportionality described by Equation 6.6. The plot clearly shows that  $Q_{lost}$  increases with  $Q_{dep}$  at all temperatures. It also illustrates a large scatter at low values of  $Q_{dep}$

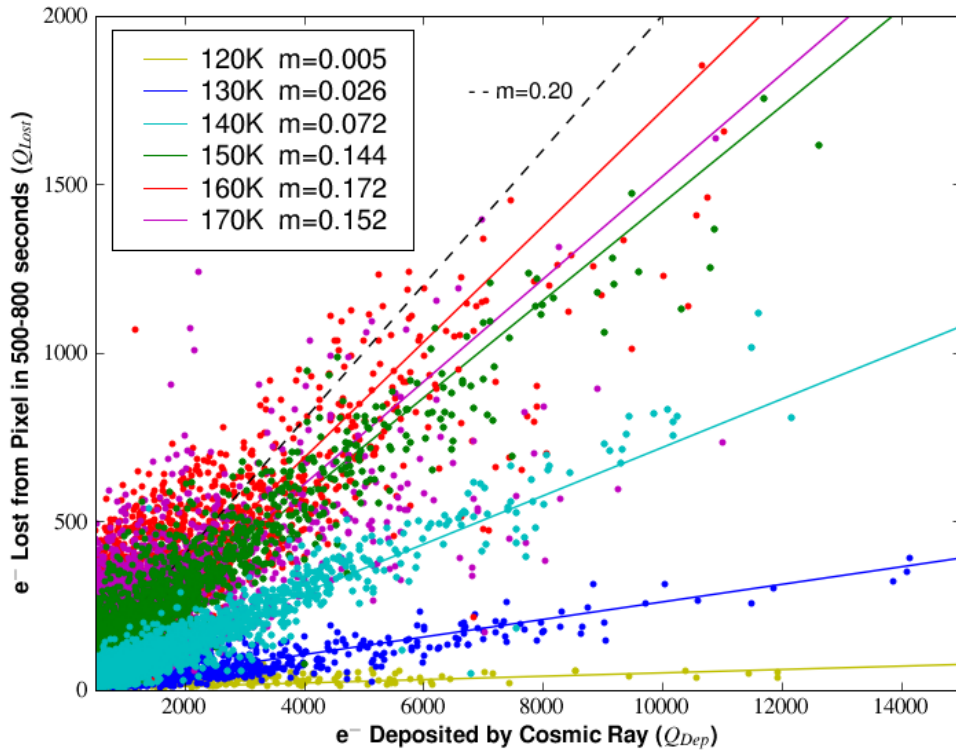


Figure 6.2: Scatter plot showing the amount of charge lost by a pixel vs. the amount of charge initially recorded in the pixel after a cosmic ray hit. The hits are chosen such that the time between the hit and the last measurement in the ramp is about 500-800 seconds. The lower limit to the x-axis is  $500 e^-$ . The temperature and slope of each line is indicated in the legend and the black dotted line shows the slope of  $m = 0.2$ . Note that, although covered by the foreground plots, the scatters of the points at temperatures above 160 are very large at lower x values.

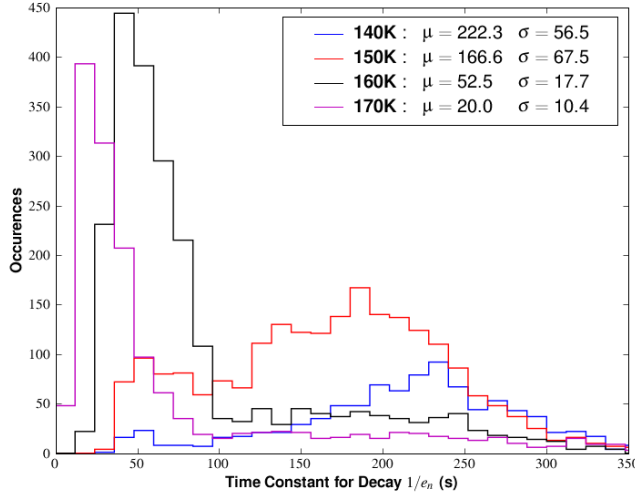


Figure 6.3: Histograms of the time constant,  $1/e_n$ , for the decay of signal after impact by a cosmic ray at temperatures between 140 and 170 Kelvin. The decays were measured in 1060 second dark exposures for cosmic ray hits that occurred in a time interval 200-500 seconds after the start of the exposure. The mean time constant,  $\mu$ , and standard deviation,  $\sigma$ , are indicated in the legend for each temperature.

for temperatures above 160 K. The most reasonable explanation for the scatter is that the delay between the hit and the first time the pixel is read results in a large discrepancy between  $Q_{dep}(t=0)$  and  $Q_{meas}$ . This explanation is supported by analysis of  $\text{Fe}^{55}$  events, which will be presented in the following section, and darks taken in window mode with a frame time of  $t = 1.6$  s. Although the amount of cosmic rays observed in window mode is very limited due to the small amount of surface area in the window, the value of  $m(T)$  at 170 K is observed to increase to about  $m = 0.20$  and the scatter is reduced. The dashed line in the plot shows this slope.

For temperatures below 140 K, the decay time may be considerably larger than 800 seconds, so there is some question as to whether the ratio  $m(T)$  accounts for all of the charge that will be lost before the pixel begins to integrate in the positive direction. For example, if the exposure was allowed to continue for 1 hour, it is possible that at 130 K the ratio of  $Q_{lost}/Q_{dep}$  would increase to the maximum value of  $m = 0.20$  observed at higher temperatures. However, as shown in the legend of Figure 6.3, the mean time constant  $\mu_{e_n}$  at 140 K is short enough to allow at least 80% of the charge to decay in 500 seconds. And the histograms in the plot show that above 140 K, the time constants rapidly decrease with increase in temperature, so there is more than enough time for the full decay to take place in 500-800 seconds. Thus, it can be concluded that the decrease in  $m(T)$  for lower temperatures is not simply a result of cutting off the integration before the decay has ceased, but rather that **less charge is effectively lost by the pixels at lower temperatures.**

### 6.1.2.3 Effect on Dark Rate and Spatial Dependence

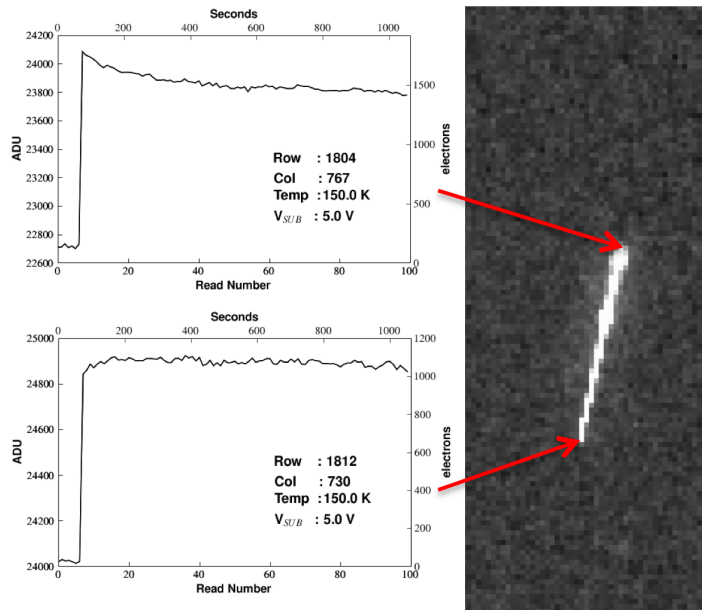
There are several other notable trends in the data that may provide some insight into the physical origin of the charge decay. One very interesting trend seen in the decays at temperatures where the

dark current is greater than about  $0.5 \text{ e}^-/\text{s}$  (almost exclusively for temperatures above 150 K) is that the dark rate changes after the decay. In some cases it increases and in other cases it decreases after the nonlinear decay subsides and the signal rate once again becomes linear. The change is typically no more than  $\pm 0.2 \text{ e}^-/\text{s}$ .

Another noteworthy point is that the pixels tend to lose the least amount of charge near the edges of the detector. Although only a handful of these events are present, about nine out of ten of them do not show signal decay, even for large values of  $Q_{dep}$ . Pixels that were less than 150 pixels away from the perimeter of the detector were intentionally left out of the plots in Figure 6.2 for this reason.

Finally, by examining the decays for long muon tracks when the detector is not fully depleted, it appears that the charge loss is dependent on the depth of interaction in the detector. Pixels at the narrow end of the track—where the muon crossed the front side—lose almost no signal at all or gain signal. The pixels at the wide end of the track—where the muon crossed the back side and generated electrons in the field free region—see a decay that exhibits the average values of  $m$  and  $e_n$ . This is depicted in Figure 6.4, which shows the ramps for two pixels at opposing ends of a muon track. Knowing which side of the detector the muon entered, and assuming that it ionizes electrons throughout its passage in the detector, one can approximate the depth at which it passed over a given pixel. Taking  $z = 0$  as the front side of the detector, if the muon entered the detector at  $(x_o, y_o)$  and left a track of length  $L_{track}$ , the depth at which it passed over the pixel at  $(x, y)$  is given

Figure 6.4: The pixels affected by long muon tracks (image at right) show a dependence of charge loss on distance along the track, which is directly related to the depth of the muon in the detector when it passed through. The image was taken with an underdepleted detector ( $V_{SUB} = 5 \text{ V}$ ), so the depth can be mapped to the width of the track. (Top left) Pixels near the back side show the typical loss and decay rate. (Bottom left) Pixels near the front side (closest to the  $\text{p}^+$  implants) show very little signal loss, and in some cases, a gain in signal.



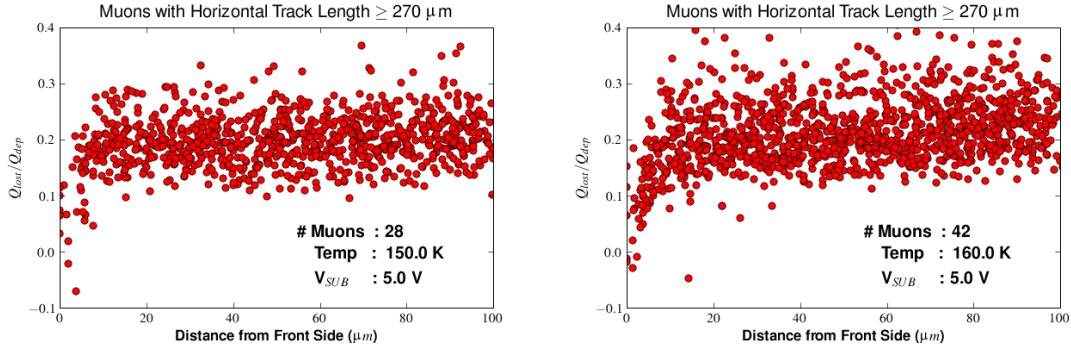


Figure 6.5: Both plots show the ratio of  $Q_{lost}/Q_{dep}$  against the calculated depth of interaction (see text) for extended muon tracks that had a clear disparity in width at opposing ends of the track. A negative ratio indicates that the pixels actually *gained* charge, evidenced by a nonlinear increase in signal after the muon hit. The number of muons sampled, along with the temperature and substrate voltages are listed in the plots.

by

$$z = \frac{\sqrt{(x - x_o)^2 + (y - y_o)^2}}{L_{track}} \times 100\mu\text{m}. \quad (6.8)$$

As part of the search algorithm described above, this calculation was carried out on all of the cosmic ray events classified as muons for which a clear disparity in width at opposing ends of the track existed. Figure 6.5 shows the results for the muon tracks that had a track length greater than 14 pixels (252 microns) at temperatures of 150 and 160 K. The figures clearly show that the charge loss is diminished for pixels at locations near to where the muon passed through the front side of the detector ( $z = 0$ ). A negative ratio  $m$  corresponds to the pixels gaining a positive charge  $Q_{lost}$  as opposed to losing  $Q_{lost}$ , which indicates that some of them gain holes instead of losing them. At a depth of  $\sim 10 \mu\text{m}$ , the ratio is seen to level off around  $m = 0.20$ . This might suggest that lateral diffusion of holes into the gaps between the  $p^+$  implants plays a strong role in the charge loss and a threshold height  $z_{threshold}$  exists where the lateral diffusion brings the charge carriers all the way into the neighboring pixels. But interestingly, the data at 160 K shows a slight positive slope all the way up to  $z = 100 \mu\text{m}$ .

When the detector is fully or over-depleted ( $V_{SUB} > \sim 7 \text{ V}$ ), there is no diffusion region at the back side of the detector and in many cases it is no longer possible to discern which end of the muon track is which based upon the width. However, the same trend of the pixels at one end losing very little charge and at the other end losing the average still exists. The effect is still strong all the way up to 20 volts; higher voltages were not examined.

### 6.1.2.4 Transfer of Charge Between Pixels

There is evidence that the charge lost in the decays is not simply leaving the detector through the backside contact or recombining in the detector, but that it is being electrically transferred to neighboring pixels. When a decay occurs in a particular pixel, often times one or more neighboring pixels see an opposing rise in signal. Without exception, the overall signal in the pixel that decays is larger than the signal in the pixel that rises. And in nearly all cases observed, the pixels that lose holes lie at the center of the event and the ones that gain holes lie near the boundary. An example is shown in Figure 6.6. Note that this response cannot be attributed to interpixel capacitance. If the coupling was governed by IPC, all neighboring pixels should see signal shifts in the same direction [24].

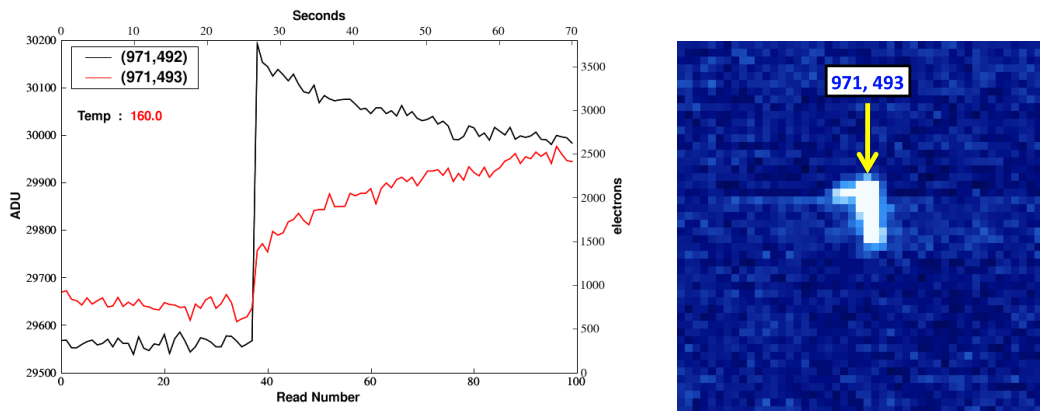


Figure 6.6: (Left) The ramps of two pixels hit by a cosmic ray. The plot in black shows the pixel that absorbed and then lost the most charge. The plot in red shows its nearest neighbor, which appears to be the recipient of some of the lost charge. (Right) Difference image of read before and after cosmic ray hit from an illuminated exposure with  $V_{SUB} = 3.0$  V. The arrow points to the pixel at (971, 493) and the one below it is (971, 492).

One might imagine that this coupling mechanism is taking place in the ROIC. For instance, the electronics might be coupling the analog output of neighboring pixels due to settling effects. However, in cases where the cosmic ray hits at the edge of the detector, an example of which is shown in Figure 6.7, no evidence of any charge sharing between the science pixels that integrate the charge dumped by the cosmic ray and their neighboring reference pixels is seen. If the charge sharing was taking place in the multiplexer then coupling between the science and reference pixels should be observed. We therefore conclude that **IPCT must occur in the photosensitive detector layer or in the oxide layer.**

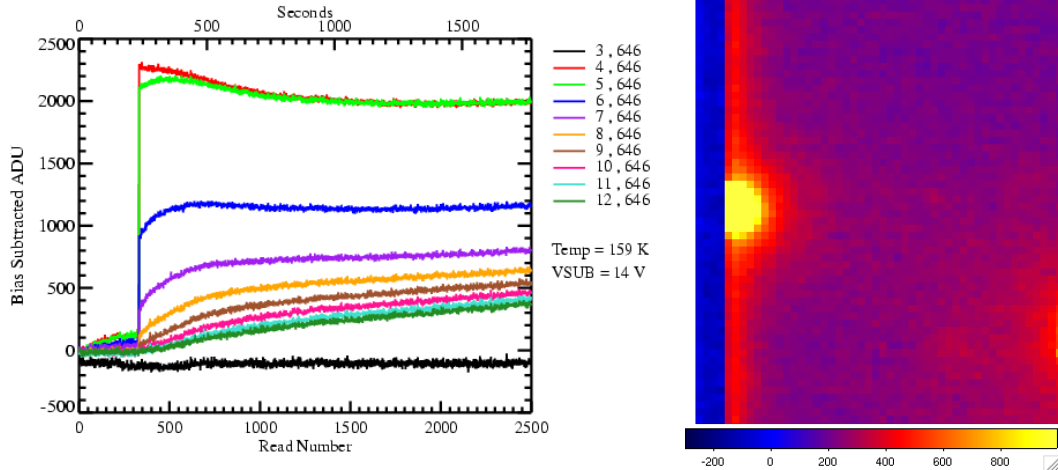


Figure 6.7: (Left) The ramps of nine pixels in order of increasing  $x$  value during an exposure where a large event occurred. The pixel with  $x=3$  is a reference pixel. It shows the same behavior as all other reference pixels in nearby rows and columns but does not show any coupling to the science pixel after the accumulation of charge from the large cosmic ray event. (Right) The last minus first read of the integration from which the ramps were taken. The image shows that this event was a very energetic one, probably induced by an x-ray or gamma ray.

### 6.1.2.5 Physical Explanations

Based upon the temperature dependence of  $m$  and  $e_n$ , the depth dependence of  $Q_{lost}$ , and the more subtle effects just described, we suggest the following explanation for what is physically happening in the detector. A fraction of holes generated by the cosmic ray are trapped at the Si-SiO<sub>2</sub> interface. Holes that were generated high above the pixel implant at an  $x, y$  location offset from the pixel reach these traps more easily than those generated very near to the implant because the vertical electric field gives them a high velocity, making it more difficult for the horizontal field near the implant to “steer” the hole directly to the implant. The trapped holes cause a rise in the signal for p<sup>+</sup> implant to which they are closest. When emitted from the traps, the holes may drift away from this implant if there is a conductive channel near the surface. Based upon Gauss’s law and the relationship between the electric field and potential (see Section 7.5), the potential (signal) at the implant will decrease as the hole moves further away. At the same time, the pixel towards which it is moving will see an increase in potential (signal).

The ease with which this happens will depend on the number of available hole traps ( $E_T < E_F$ ), which will go like  $\exp([E_T - E_F]/kT)/(1 + \exp([E_T - E_F]/kT))$ , and the trap capture coefficient, which goes like  $T^{1/2}$ . The trapping rate efficiency will thus increase with increasing temperature, and the detrapping time will get smaller. This model is further supported by the fact that IPCT was greatly reduced in H2RG-148 after the Si-SiO<sub>2</sub> surface was treated differently during fabrication.

### 6.1.3 Measurement via Fe<sup>55</sup>

Ionizing radiation provides a means to measure the coupling between neighboring pixels in a detector. Figer et al. [65] use cosmic ray events in up the ramp dark exposures to measure the compounded effect of charge diffusion and incomplete settling on pixel crosstalk. And as mentioned in Section 6.1.2.3, muon tracks can be used to directly measure charge diffusion since the entry and exit point of the particle are known. However, since cosmic rays come from a whole host of sources [108] and sample a large, nonuniform energy spectrum, it is not possible to determine the depth at which the particle interacted in the detector or cross check the number of electron hole pairs generated against the energy of the incident particle.

An x-ray source like Fe<sup>55</sup> solves these problems since the energy spectrum, and thus, the absorption depth and number of electron-hole pairs generated in the silicon is well known (approximately 30  $\mu\text{m}$  for the Mn x-ray photon).<sup>2</sup> The following sections describe a method for precisely measuring pixel crosstalk with an x-ray source such as Fe<sup>55</sup>. Section 6.1.3.3 shows results that are typically associated with diffusive crosstalk and IPC and Section 6.1.3.4 addresses the role IPCT plays in Fe<sup>55</sup> measurements.

#### 6.1.3.1 Data Collection

The experimental setup used to collect the Fe<sup>55</sup> data is the same as the one described in Section 4.3. The data collected for H2RG-32-147, H1RG-022, and H4RG-10-007 in the RIDL dewar were not used to measure crosstalk because they had an RMS read noise of  $\sigma_{rn} = 20\text{-}50\text{ e}^-$  per pixel. The signal to noise ratio for these Fe<sup>55</sup> events thus prevents us from distinguishing the  $K_\alpha$  and  $K_\beta$  peaks. For H2RG-001, the read noise was greatly improved due to the changes described in Section 4.4.  $\sigma_{rn}$  ranged between 7-10  $\text{e}^-$ , which is less than the Fano noise of  $\sigma_{Fano} = 13\text{ e}^-$ , and this allows us to separate the peaks. With H2RG-001, several days worth of data were collected at temperatures ranging from 90-180 K in 10 K increments, and ample time was taken for the detector to stabilize after each temperature change. Lastly, backside voltages of  $V_{SUB} = 25\text{ V}$  and  $V_{SUB} = 40\text{ V}$  were used.

#### 6.1.3.2 Data Analysis

Analysis of the Fe<sup>55</sup> data consists of a *guess and check* method to determine pixel crosstalk. We *guess* the amount of crosstalk between nearest neighbors and *check* to see if the energy spectrum is well represented. At the estimate that most closely matches the actual physical crosstalk, the Fe<sup>55</sup> peaks should be best resolved. If the estimate is far off, the peaks will blend together as one.

The crux of this method is the assumption that a small fraction of the Fe<sup>55</sup> events in the data are *single pixel events*. That is, the initial electron cloud is centered directly above, and close enough

---

<sup>2</sup>The absorption depth of a given particle in a given material is defined as the depth in a material at which 1-1/e of the incident particles in a large distribution have been absorbed.

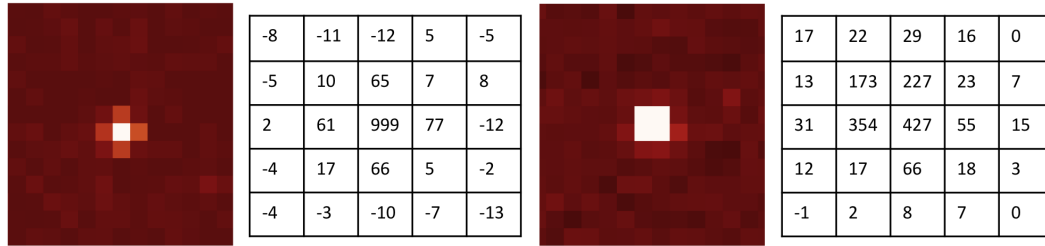


Figure 6.8: Representative examples of single (left) and multiple (right) events generated from exposure to  $\text{Fe}^{55}$  source. The tables to the right of the images show the  $5 \times 5$  set of raw ADU values surrounding the pixel with the maximum value (after bias subtraction).

to, the pixel collection node that all of the  $1620 \pm 12.7$  holes generated by a  $K_\alpha$  x-ray or  $1770 \pm 13.3$  holes generated by a  $K_\beta$  x-ray are collected by that pixel. Figure 6.8 illustrates the difference between a single pixel event and a multiple pixel event. In the single pixel event, to first order crosstalk occurs only between the pixel that collected the charge and its eight nearest neighbors. In the multiple pixel event, this number grows because more than one pixel has collected charge.

Identifying single pixel events once the crosstalk percentages are known is a very straightforward process. If the crosstalk is not known, one must iterate through potential values using the guess and check method described above. The steps in going from a three dimensional datacube to obtaining the crosstalk values are described below.

**1) Form 2-d hit images** For a datacube with reads  $r = 0, 1, \dots, R$ , where  $R$  is the last read,  $R - 1$  difference images are formed by subtracting consecutive frames. The pixel values in the  $r^{\text{th}}$  difference image yield the amount of charge deposited by the x-rays that hit between the reads  $r - 1$  and  $r$ . One might argue that averaging the pixel value over the reads before the hit and averaging the pixel values after the hit and using this difference will yield better signal to noise. However, as will be shown in Section 6.1.3.4, at temperatures above 120 K the signal of a hit pixel decays in the reads following the hit. Averaging the values after the hit for these temperatures therefore increases the uncertainty in the amount of charge deposited by the x-ray.

**2) Identify contiguous sets of pixels** Each 2-d image is first masked so that all bad pixels have their values set to 0. The images are then searched for contiguous sets of pixels that have a value greater than  $3\sigma_{rn}$ . For each contiguous set, the total number of pixels that meet this criteria along with the largest pixel value and the values of its eight nearest neighbors are recorded to a MySQL database. To be clear, this means that even if only two pixels in a contiguous set are above  $3\sigma_{rn}$ , nine pixel values will be stored. This allows for measurement of crosstalk below the  $3\sigma_{rn}$  level. Also recorded are the location of the peak pixel, its read number, and other tracking information such as bias voltage, temperature, and the name of the file in which it was found.

**3) Iterate over potential crosstalk values** Once all events are recorded, trial crosstalk values can be used to search the database for single pixel events. A lower threshold for the maximum pixel value, obtained by inspecting a handful of events, is also used in the search to ensure that only  $K_\alpha$  and  $K_\beta$  events are returned. Queries are only made for entries that had nine or less contiguous pixels since more than nine pixels indicates a double hit. For each query, the returned pixel values are ordered by their position in the  $3 \times 3$  box surrounding the central pixel, as this is how they were stored.

The crosstalk values, or coupling constants,  $\alpha_{x,y}$ , are defined relative to the intensity of the central pixel,  $S_{0,0}$ . The pixel immediately to the left of center will have a value  $S_{-1,0} = \alpha_{-1,0}S_{0,0}$ , the pixel in the upper right corner will have a value  $S_{1,1} = \alpha_{1,1}S_{0,0}$ , and so on. For notational convenience, the left and right coupling constants are expressed as  $\alpha_{\pm 1,0}$ , the top and bottom as  $\alpha_{0,\pm 1}$ , and the diagonals as  $\alpha_{\pm 1,\pm 1}$ .

The queries are made by demanding that, in addition to the constraints on  $S_{0,0}$  and the number of pixels discussed above, the coupling constants fall within certain ranges  $\alpha^{min}$  to  $\alpha^{max}$ :

$$\begin{aligned} \alpha_{\pm 1,0}^{min} < \alpha_{\pm 1,0} < \alpha_{\pm 1,0}^{max} \\ \alpha_{0,\pm 1}^{min} < \alpha_{0,\pm 1} < \alpha_{0,\pm 1}^{max} \end{aligned} \quad (6.9)$$

At each  $\alpha$  range, the returned single pixel ADU values are binned and an attempt to detect the  $K_\alpha$  and  $K_\beta$  is made. If the attempt fails, the range is ruled out of consideration. If the attempt succeeds, a minimum  $S_{0,0}^{min}$  between the two peaks at  $S_{0,0}^{K_{alpha}}$  and  $S_{0,0}^{K_{beta}}$  is determined. The widths of the two peaks is then approximated by taking the second moment of the distributions from the range of ADU values extending a distance of  $\Delta K_\alpha = S_{0,0}^{min} - S_{0,0}^{K_\alpha}$  to the left and right of the  $K_\alpha$  peak, and a similarly defined range around the  $K_\beta$  peak. The parameter finally used to compare different  $\alpha$  values is the ratio of the peak heights to the peak widths. Note that the bin size must be set appropriately small ( $\sim \sigma_{rn}/2$ ) to ensure the growth of the peak does not overwhelm the growth of the width.

Starting at  $\alpha^{min} = 0$  and  $\alpha^{max} = 0.045$ , which corresponds to a range of slightly more than  $\pm 2\sigma_{rn}$ , the values are incremented by 0.01 in parallel. Once a clear minimum in the peak height to width ratios is found, for example  $\alpha_{min} = 0.05$  and  $\alpha_{max} = 0.095$ , finer adjustments in the  $\alpha$  values are made and the range is adjusted. Also,  $\alpha_{\pm 1,0}$  and  $\alpha_{0,\pm 1}$  are varied independently if a clear asymmetry is present in the two directions. Some example values from the iteration process performed on the Fe<sup>55</sup> data taken with H2RG-001 at 160 K and  $V_{SUB} = 25$  V are shown in Figure 6.9. It is again emphasized that the three distributions in the figure are drawn from the same parent distribution of events. They only differ because of the constraints listed in Equation 6.9. The upper left plot is a distribution that constrains the crosstalk to be too small, the lower left one constrains it to be too large, and the right one constrains the crosstalk to most closely match the actual value.

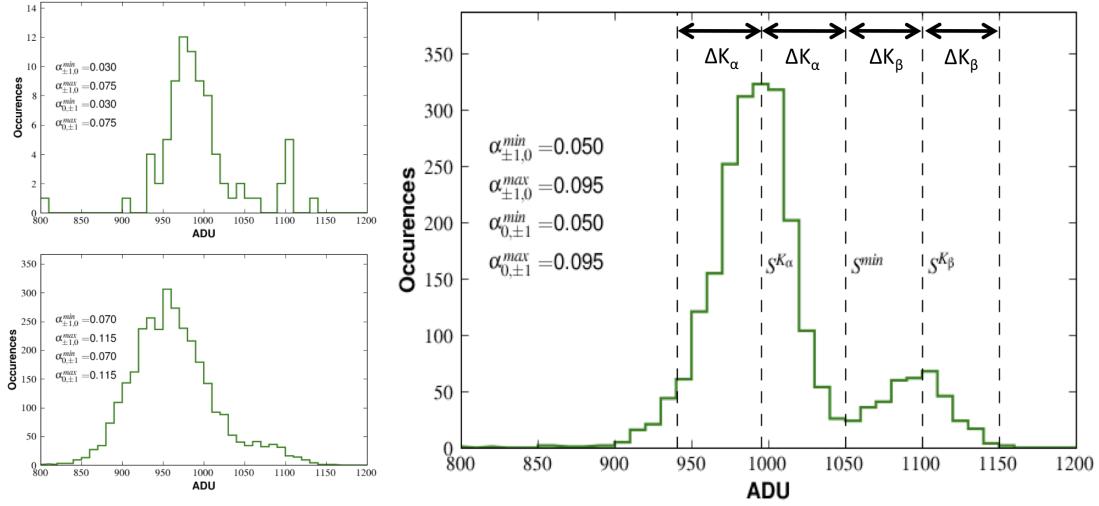


Figure 6.9: Example distributions obtained with the guess and check method for crosstalk values too low (upper left), too high (bottom left), and properly centered (right). In the right diagram, the quantities  $S_{0,0}^{K_\alpha}$ ,  $S_{0,0}^{min}$ , and  $S_{0,0}^{K_\beta}$  are shown with the 0,0 omitted. Also shown are the widths used to calculate the seconds moments  $\Delta K_\alpha$  and  $\Delta K_\alpha$  as well as the crosstalk values,  $\alpha$ , that were used to find single pixel events.

### 6.1.3.3 Results

The results for measurements made between 100 K and 170 K with the detector operating in Full Frame mode ( $t_{frame} = 10.6$  s) are shown in Table 6.1 and Figure 6.10. The most noticeable feature in the plot is the large jump in crosstalk values at 130 K. While not fully understood, this is believed to be the same phenomenon mentioned in Section 4.3.7.1, which affects the conversion gain and voltage offsets of the pixels (presumably as a result of an offset on the output of the pixel source follower).

Aside from the large jump, the coupling values are relatively stable as the temperature increases. The slight increase in coupling with increase in temperature above 130 K may be a result of lateral charge diffusion, which goes like  $\sqrt{T}$ . Ideally, lateral charge diffusion should be negligible since the data points represent single pixel events and it is assumed that none of the holes generated in the initial charge cloud are collected by the surrounding pixels. In other words, all of the crosstalk is assumed to be due to IPC or any other form of electric crosstalk. However, even if the holes from the charge cloud do not make their way to the neighboring pixels, which would cause an increase in their signal and a resulting increase in  $\alpha$ , some may make their way to the surface surrounding the collecting implant, causing a deficiency in the charge measured in the center pixel. The latter would also cause an increase in  $\alpha$ .

The asymmetry between the vertical and horizontal neighbors is not fully understood, but has

been measured in previous studies of infrared and visible hybrid devices [111, 52]. No known asymmetry exists in the layout of pixels in the detector material, so this would lead one to the conclusion that it must be caused by the multiplexer. However, Moore found no substantial evidence of asymmetry—or coupling at all for that matter—in a bare multiplexer [24]. This suggests the higher voltages present at the gates of the pixel source followers brought about by the use of the backside contact voltage (and corresponding current draw) are partly responsible. The horizontal neighbors could possibly be coupled more strongly by either the read control line or reset control line shared by pixels in a common row. There is a discrepancy between the left and right  $\alpha$  values that is constant with temperature, suggesting it is not a result of the  $\text{Fe}^{55}$  source being off-center. All of these discrepancies require further investigation.

In addition to the coupling values, the analysis provides a ratio for the number of single pixel  $K_\alpha$  and  $K_\beta$  events to the total number. Table 6.1 shows that this number ranges from 0.016-0.027 over the temperature range tested. While this number may seem small, the following argument shows that it is reasonable. In order for the holes in the charge cloud to be completely absorbed by a single pixel, it must be generated sufficiently deep in the detector to prohibit loss of carriers by lateral diffusion. The absorption depth of the Mn x-rays is  $30 \mu\text{m}$ , so the fraction  $f_D$  that make it to a depth  $D$  in the detector (measured from the illuminated backside) is

$$f_D = e^{-D/30 \mu\text{m}}. \quad (6.10)$$

The charge cloud should also be generated directly overhead the  $\text{p}^+$  collecting node or else diffusion to neighboring pixels or loss to traps in the gaps will take place. The fraction of these events will go like

$$f_A = A_{\text{implant}}/A_{\text{pixel}}, \quad (6.11)$$

where  $A_{\text{implant}}$  is the area of the highly doped implant and  $A_{\text{pixel}}$  is the total area of pixel. The fraction of single pixel events measured at depth  $D$  should be the product of these two factors:

$$f_{sp} = f_A f_D = \frac{A_{\text{implant}} \cdot e^{-D/30 \mu\text{m}}}{A_{\text{pixel}}} = \frac{l_{\text{implant}}^2 \cdot e^{-D/30 \mu\text{m}}}{l_{\text{pixel}}^2} \quad (6.12)$$

The rightmost expression assumes both the pixel and implant have a square shape with length  $l$ . While the pixel is known to be square with  $l_{\text{pixel}} = 18 \mu\text{m}$ , the actual geometry of the implant and its size are proprietary and not known. But assuming that single pixel events are generated at a depth between  $D = 90 - 99 \mu\text{m}$  and using  $\overline{f_{sp}} = 0.0227$ , we obtain  $12.1 \mu\text{m} < l_{\text{implant}} < 14.0 \mu\text{m}$ . This is a reasonable value for the dimensions of the implant, which suggests that the fraction of single events measured is a realistic number.

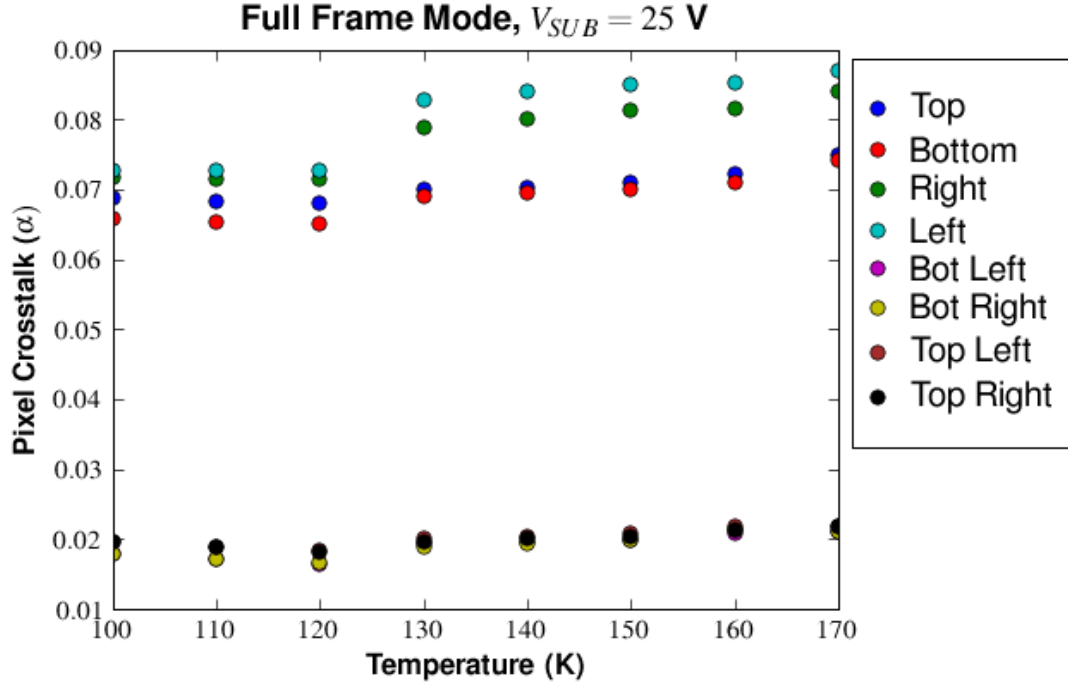


Figure 6.10: Crosstalk values vs. temperature for H2RG-001 measured from single pixel  $\text{Fe}^{55}$  events. The details of the bump and disparity between the nearest neighbors are explained in the text.

Table 6.1: Pixel crosstalk parameters for H2RG-001. The discrepancy in the total event numbers is a result of uneven sampling at different temperatures. The large conversion gain at  $T=170$  K is due to IPCT (discussed in Section 6.1.2).

Temperature	Total Events	Single Pixel Events	Fraction	Conversion Gain
100	475,286	12,785	0.0269	1.141
110	546,693	13,298	0.0243	1.125
120	541,769	11,446	0.0211	1.080
130	510,669	12,147	0.0237	1.149
140	491,390	11,521	0.0234	1.157
150	448,881	10,186	0.0227	1.149
160	313,070	4,917	0.0157	1.165
170	111,782	2,357	0.0211	1.280

### 6.1.3.4 Charge Loss in Fe<sup>55</sup> Measurements

One of the areas where Interpixel Charge Transfer (IPCT) shows most impact is in the measurement of conversion gain through the use of Fe<sup>55</sup>. Unlike the trails of electron-hole pairs left by minimum ionizing particles and wandering recoil electrons generated by stray gamma ray events, the 5.9 keV x-ray photons emitted from the Fe<sup>55</sup> source generate 1620 e<sup>-</sup> contained within a diameter of only 0.4  $\mu\text{m}$  [3], so it is not immediately obvious that the charge decay will exhibit the same characteristics. But as Figure 6.2 shows, for charge deposits in the range of 1000-2000 e<sup>-</sup>, there will be a significant amount of holes—in most cases greater than the CDS read noise of the detector—lost by the pixels that integrated the deposit. And as with the cosmic ray events, the effect will be more pronounced at lower substrate voltages, slow frame rates, and higher temperatures, especially at temperatures above 140 K. It will now be shown that the charge decay can have a detrimental impact on x-ray energy measurements.

As an illustrative example of the decay after Fe<sup>55</sup> hits, Figure 6.11 shows the ramps of two pixels from an exposure where H2RG-32-147 was exposed to the Fe<sup>55</sup> source. The decay in signal after a single hit or multiple hits is evident in the ramps, and it effectively appears as a decrease in the signal for that pixel. The dark current rebounds after a few time constants  $1/e_n$ . However, as with cosmic rays, in most cases it does not return to the same rate as before the hit, and the direction of change seems to depend on the conditions in neighboring pixels.

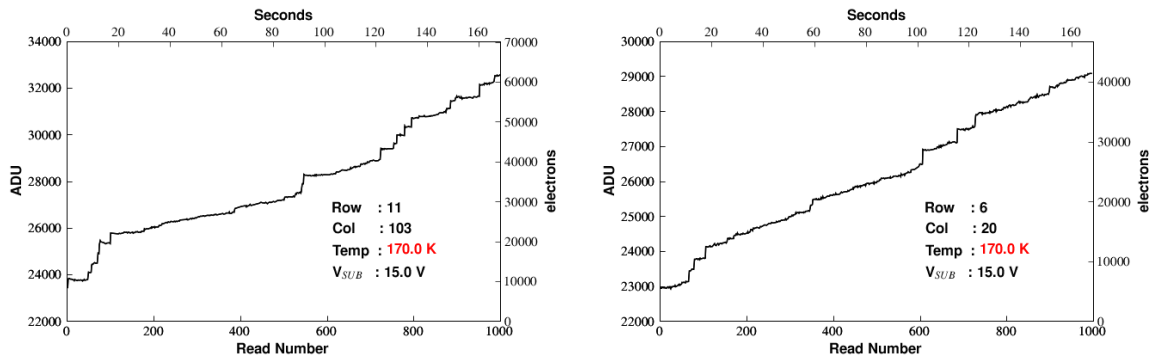


Figure 6.11: Two ramps taken with H2RG-32-147 in window mode while it was exposed to the Fe<sup>55</sup> source. After a hit (or multiple hits) the pixel loses a small fraction of signal, resulting in an apparent decrease in signal. The charge in the pixel before the source follower voltage is read may be slightly greater than the amount of charge present when it is actually read, resulting in an incomplete sample of the electrons deposited by the x-rays.

As discussed in the previous section, because the sampling rate of a given pixel is not infinitesimally small, at certain temperatures the pixel will have lost a significant amount of charge between the time the x-ray hit,  $t_{hit}$ , and the time the pixel is read,  $t_{read}$ . This is a source of systematic error since there is uncertainty in the quantity  $\Delta t = t_{read} - t_{hit}$ . The events occur with a uniform

probability in time,  $P(t)$ , and  $\Delta t$  can vary between  $\Delta t = 0$ , where the pixel is read before any charge has been lost and,  $\Delta t = t_{frame}$ , where the pixel is read nearly an entire frame time after it has been hit. The latter case will lead to the largest measurement error.

The amount of “missing charge” and its dependence on temperature can be estimated by using the empirical results from Section 6.1.2. If the pixel will lose a total amount of holes  $Q_{lost}$  during the exponential decay (note that this cannot be stated as  $t \rightarrow \infty$  since the dark current takes on a different value after the decay in some cases), then the amount of charge it will lose in  $\Delta t$  is

$$q_{lost} = Q_{lost}(1 - e^{-e_n(T)\Delta t}), \quad (6.13)$$

And as shown by Figure 6.2, the total amount of holes lost during the decay can be roughly approximated by a linearly relationship to the amount of holes deposited by the x-ray:<sup>3</sup>

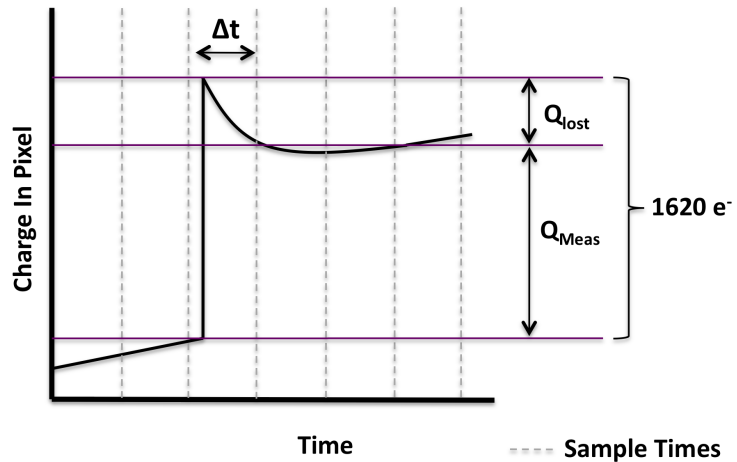
$$Q_{lost} = Q_{dep} \cdot m(T) \quad (6.14)$$

So the relationship between the measured charge and the charge deposited is

$$Q_{meas} = Q_{dep}[1 - m(T)(1 - e^{-e_n(T)\Delta t})]. \quad (6.15)$$

This equation shows that measured signal charge decreases with  $\Delta t$  and increasing temperature since  $m(T)$  is an increasing function of  $T$ . Figure serves to 6.12 illustrates this. There are two important consequences of the charge loss:

Figure 6.12: A pictorial plot that shows the behavior of pixel signal vs. time before and after an  $\text{Fe}^{55}$  x-ray has struck at temperatures higher than about 130 K. The bottom horizontal line shows the signal before the event and the top one shows the signal after the hit. The middle horizontal line shows the signal a time  $\Delta t$  after the hit, when it is sampled. The quantity of charge  $Q_{lost}$  is lost before the read, so that  $Q_{Meas}$  is measured.



<sup>3</sup>For other events generated by ionizing radiation, the relationship between the charge lost and the charge deposited for a given pixel is dependent on the position of the pixel in the event as a whole and the substrate voltage.

1) **The  $K_\alpha$  and  $K_\beta$  lines will be measured at a lower ADU value,** resulting in an underestimate of the x-ray energies and an overestimate of the conversion gain (more  $e^-$  per ADU). Because the events occur with a uniform probability of  $1/\Delta t$  in time, the mean value of the charge lost when measuring with a sample interval  $\Delta t$  will be:

$$\langle q_{lost} \rangle = Q_{lost} \left( 1 - \int_0^{\Delta t} \frac{e^{-e_n t}}{\Delta t} dt \right) = Q_{lost} \left( \frac{e^{-e_n \Delta t} - 1}{e_n \Delta t} + 1 \right) \quad (6.16)$$

The peaks will shift by this amount relative to a measurement where  $\Delta t \rightarrow 0$ , which represents the case when the interval between successive samples of the pixels is very small.

2) **The width of both peaks will increase** due to the uncertainty in the interval of time between when the x-ray hit and when the measurement takes place. The variance in the measured amount of charge lost will be

$$\langle (q_{lost} - \langle q_{lost} \rangle)^2 \rangle = \int_0^{\Delta t} \frac{1}{\Delta t} (Q_{lost} e^{-e_n t} - \langle q_{lost} \rangle)^2 dt = Q_{lost}^2 \left( -\frac{1 - e^{-2e_n \Delta t}}{2e_n \Delta t} - \frac{(1 - e^{-e_n \Delta t})^2}{e_n^2 \Delta t^2} \right) \quad (6.17)$$

The widths of the  $K_\alpha$  and  $K_\beta$  peaks,  $\sigma_{K_{\alpha,\beta}}$ , should be increased by this uncertainty relative to the read noise,  $\sigma_{rn}$ , and Fano noise widths,  $\sigma_{Fano}$ , in quadrature:

$$\sigma_{K_{\alpha,\beta}} = \sqrt{\sigma_{rn}^2 + \sigma_{Fano}^2 + \sigma_{IPCT}^2}, \quad (6.18)$$

where  $\sigma_{IPCT} = \sqrt{\langle (q_{lost} - \langle q_{lost} \rangle)^2 \rangle}$ , and the *IPCT* subscript indicates the noise is due to charge loss/transfer. Although the peak widths will not be symmetric around the mean (due to the fact that the decay is more likely to be sampled near the bottom), an approximation of the full width at half maximum (FWHM) can be made with  $FWHM = 2.354\sigma$ . When the peaks begin to encroach one another for high  $T$  and long  $\Delta t$ , an obvious consequence will be that they are no longer resolvable as separate peaks.

Equations 6.16 and 6.17 are plotted in Figure 6.13, and agree very well with the data. Below 160 K, a degradation of the  $\text{Fe}^{55}$  spectrum is not seen for the lowest sampling rate of  $t_{frame} = 10.6$  s used to collect the data. This is expected since the time constants at these temperatures for the charge loss are much greater than the frame time. The peaks shift only slightly and the widths are dominated by the read and Fano noise. However, the effect begins to degrade the spectrum at 160 K where the time constant approaches 50 seconds and is seen quite dramatically at 170 K, as illustrated by Figure 6.14. At this temperature, if a Mn  $K_\alpha$  x-ray deposits all of its charge in one pixel and a time  $\Delta t = 10.6$  s elapses before the pixel is read (this is the time for an H2RG frame when reading out of four outputs), it will have lost approximately 133  $e^-$  (114 ADU). This is more than thirteen times as large as the read noise. On average the measured charge will be 92  $e^-$  (80

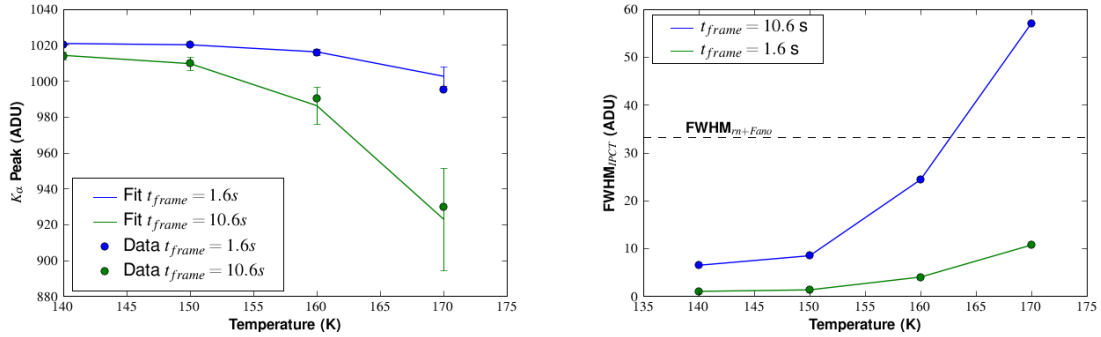
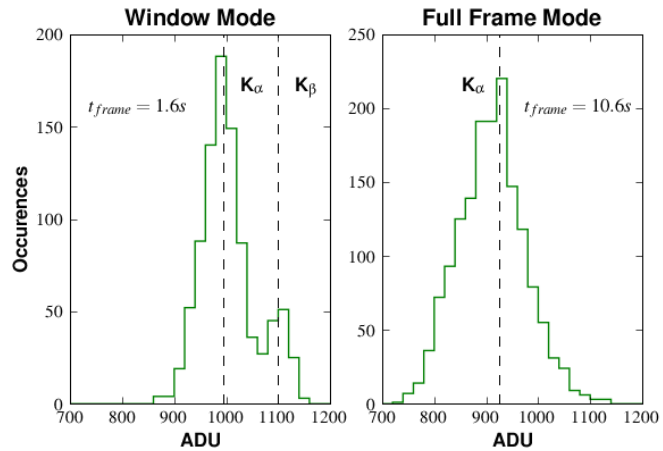


Figure 6.13: (Left)  $K_\alpha$  ADU value for the center pixel in single pixel  $Fe^{55}$  hits from measurements taken in full frame mode with a frame time of 10.6 seconds and window mode with a frame time of 1.6 seconds. The data is shown by the circles and the predicted peak shift (assuming  $Q_{dep}(t=0) = 1022 e^-$ ) from the fit in Equation 6.16 is shown by the solid lines. The error bars are determined by the uncertainty in the decay time constant  $e_n$ . (Right) The contribution of IPCT to the FWHM of the  $K_\alpha$  peak as determined by Equation 6.18. The FWHM due to the pixel read noise and Fano noise alone is shown by the black dashed line. The conversion gain for the data is roughly  $1.16 e^-/ADU$ .

ADU) less than the charge deposited, and the peak will be shifted by this amount. The observed peak shift is  $104 e^-$  (90 ADU), and the two values agree within the error due to the uncertainty in the time constant. Also, as shown by the dashed line in Figure 6.13, at 170 K and  $t_{frame} = 10.6 s$  the FWHM of each peak is dominated by the uncertainty in the charge lost. The calculation shows that the FWHM of the peaks will be about 65 ADU as opposed to 33 ADU in the case when the read and Fano noise dominate. Since they are only separated by about 100 ADU, the peaks should no longer be discernible, which is exactly what is observed in the measured spectrum.

Figure 6.14: Two histograms showing the effect of IPCT on the  $Fe^{55}$  spectra taken with a fast frame rate (left) and a slow frame rate (right). With  $t_{frame} = 1.6 s$ , both peaks are detected. But with  $t_{frame} = 10.6 s$ , the  $K_\beta$  peak is not detected. All other operating conditions used in collecting the data for the two plots (e.g.  $V_{SUB}$ , clocking speed, bias voltages, etc.) are the same.



### 6.1.3.5 Application to Soft X-Ray Measurements

HyViSI detectors are implemented, and have been proposed for future use, in x-ray astronomy and spectroscopy [25]. The calculations and data in the preceding section show that if the HyViSI detector is to be used in measuring x-ray energies below 10 keV, sufficiently low temperatures ( $< 160$  K) and short frame times should be used. Otherwise, the energies must be estimated using Equation 6.16 to account for charge loss. Even with this calibration, for high temperatures and long frame times detection of closely spaced spectral lines such as  $K_\alpha$  and  $K_\beta$  will be impossible. The operating conditions for the detector must therefore be carefully chosen. Note that new surface treatments have dramatically reduced this effect, so a preliminary inspection of each HyViSI device should be taken to see whether or not it is present at the level just described.

### 6.1.4 Measurement via Single Pixel Reset

Using the guide mode feature of the HxRG multiplexers allows one to reset or read one pixel of the array while the other pixels of the array are integrating. In an ideal detector, resetting the single pixel would not affect the neighboring pixels. However, in the HyViSI we observe that the neighboring pixels are indeed affected, either through capacitive coupling, charge injection, or oxide charging. Lateral charge diffusion before collection is eliminated as a contributor to the crosstalk since charge carriers do not traverse from the backside of the detector. The act of resetting the single pixel in guide mode also creates a persistence signal after the readout is switched back to full frame mode, which will be important for the discussions in Chapter 7. The following sections describe the experimental setup used for the Single Pixel Reset (SPR) scheme and the results. Some of the results are straightforward and have been discussed previously in the literature. Others indicate unexpected effects that have not been discussed.

#### 6.1.4.1 Experimental Sequence

To identify which mechanisms are dominant in the post-collection, electrical pixel crosstalk, we ran experiments that used the single pixel reset mode. Our measurements were made in the dark, in contrast to those made by Finger et al. [52], where the detector was uniformly illuminated. The exposure sequence used for the experiments was the following:

- 1) Reset the full array to a value  $V_{RstFF}$ .
- 2) Reset the single pixel at location  $i, j$  to a value  $V_{RstWin}$  a total of  $N_{Rsts} = 25, 50, 75,$  or  $100$  times.
- 3) Read the full frame in 32 output mode.
- 4) Repeat steps 2-3 a total of 10 times.

After these 4 steps, we performed the sequence again, but this time without applying the reset in step 2. Instead of applying the reset, the single pixel was simply clocked the same number of times—25, 50, 75, or 100—as it was in the previous sequence. Thus, the exposure time of the sequence with the reset voltage applied in step 2 is the same as the one without the reset voltage applied. This ensures that the integration time for the pixels is the same in each sequence and allows us to subtract corresponding reads in successive exposures.

We performed these sequences at 10 K increments from  $T = 100$ -180 K. At each temperature, we began with  $V_{RstWin} = 0.1$  V and then increased this voltage in the sequence  $V_{RstWin} = 0.2, 0.4, 0.6, 0.8, 1.0, 1.2, 1.4, 1.6$  V while holding  $V_{RstFF}$  at a constant voltage. We first performed this sequence at  $V_{RstFF} = 0.30$  V and  $V_{SUB} = 5$  V while moving up in temperature. Once we reached  $T = 180$  K, we increased  $V_{SUB}$  to 15 V and moved through the temperature range in a decreasing fashion. At  $T = 100$  K we increased  $V_{SUB}$  to 25 V and proceeded to increase the temperature. Lastly, once  $T = 180$  K was reached, we increased the full frame reset voltage to  $V_{RstFF} = 0.70$  V and repeated the experiment moving down in temperature.

To analyze the data, we subtracted the exposures in which the pixel was not held under reset from the ones in which it was. Since the concern is with the offset of the pixels from their value when they are all uniformly reset to the same voltage and not the integration of dark current, the bias value were used for comparison. In other words, if the signal measured after reset in the center pixel and its left neighbor are  $S_{FF}(0, 0)$  and  $S_{FF}(-1, 0)$  without the single pixel reset, respectively, and  $S_{SPR}(0, 0)$  and  $S_{SPR}(0, -1)$  are the corresponding values with the single pixel reset, then the crosstalk value for the left neighbor will be

$$\alpha_{0,-1} = \frac{S_{SPR}(-1, 0) - S_{FF}(-1, 0)}{S_{SPR}(0, 0) - S_{FF}(0, 0)}, \quad (6.19)$$

Expressions for the other neighbors are made simply by swapping indices.

#### 6.1.4.2 Expected Results

When the window reset voltage  $V_{RstWin}$  is amply greater than the full frame reset voltage  $V_{RstFF}$  ( $300 \text{ mV} < V_{RstWin} - V_{RstFF} < 800 \text{ mV}$ ), the measured crosstalk showed the trend expected from interpixel capacitance with a slight asymmetry between the fast and slow directions. As can be seen in Figure 6.15, the crosstalk values to diagonal neighbors are nearly identical to the ones obtained from single pixel  $\text{Fe}^{55}$  events. The crosstalk to the four closest neighbors, 6.9% for the fast read direction and 4.7% for the slow read direction, is significantly less, though. The measurements made by Finger et al. [52] for HyViSI devices were 8.5% in the slow and 9.3% in the fast: also significantly higher.

The source of discrepancy between these SPR results and those of Finger et al. can be attributed in part to lateral charge diffusion prior to collection at the integrating node since an illumination

source was used for their measurements and not in ours. In fact, with illumination the photogenerated holes should actually be drawn more strongly to the pixel that is reset since it presents the minimum in potential (all surrounding pixels are allowed to integrate, thereby increasing their potential and decreasing the vertical electric field). This will decrease the denominator in Equation 6.19 and make the  $\alpha$  values larger. A logical guess might be that the discrepancy with the  $\text{Fe}^{55}$  values can also be attributed to lateral diffusion or carriers that are not swept by the metallurgical junction to the collecting node. However, the next section will show that—for the top and bottom neighbors at least—the results are affected to a great degree by an overall shift in signal on the entire column of the pixel undergoing SPR.

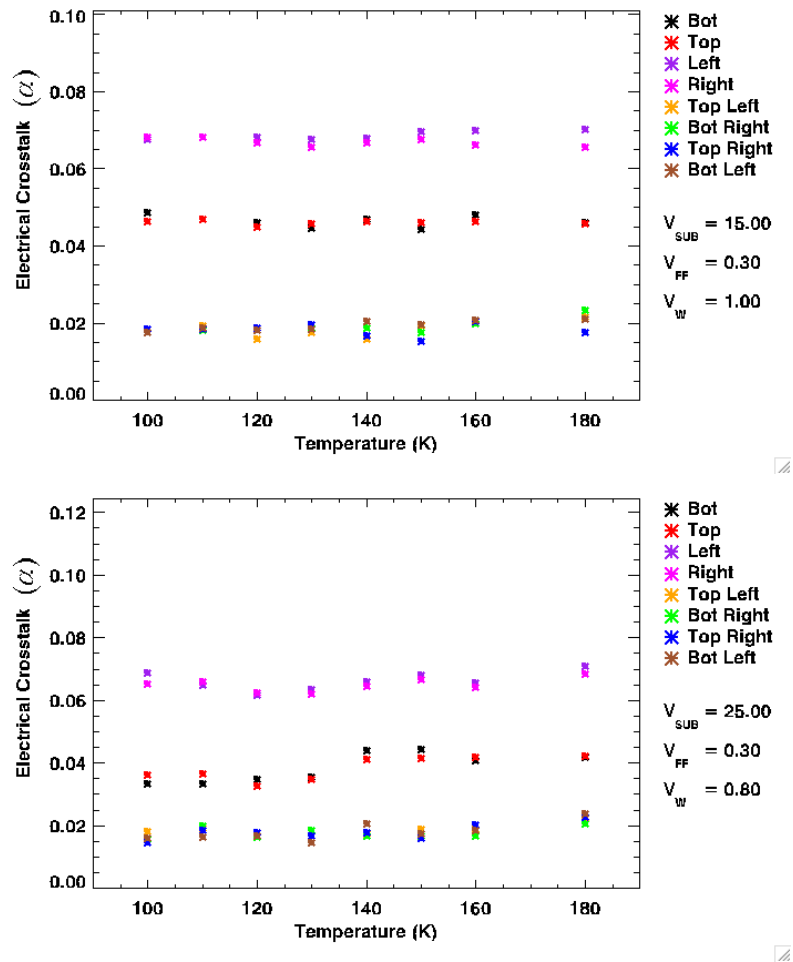


Figure 6.15: Pixel crosstalk observed in single pixel reset. The full frame is reset at  $V_{FF} = V_{RstFF}$  and the center pixel is reset continuously at  $V_W = V_{RstWin}$  while the other pixels integrate. The backside voltage is maintained at  $V_{SUB}$ .

### 6.1.4.3 Unanticipated Results

**Column Depression** The left image in Figure 6.16 shows an unexpected artifact in the SPR tests. The entire column that the single pixel belongs to suffers from a lowered voltage. The slump in voltage ranges from a few millivolts to tens of millivolts depending on the difference between  $V_{RstWin}$  and  $V_{RstFF}$  as well as the temperature. To the best of our knowledge, this phenomenon and the effect it has on IPC measurements has not been discussed in the literature. As the right plot in Figure 6.16 shows, though, its impact can be substantial.

Bezawada et al. found an increase in the DC offset along the rows of windowed pixels in an infrared HIRG [76]. It was noted that the offset is only caused by resetting the window; not reading it. However, our measurements with the H2RG HyViSI show that reading the window also causes offsets along the columns and rows. To test the possibility that the offset was a result of not properly clocking the window, extra HCLKs and VCLKS were added to the clocking sequence. The change in clocking did not remove or reduce the offsets.

The offsets are not entirely a surprise; it is a well known fact that changing clocking patterns in CMOS detectors can cause such behavior. But the role this plays in the asymmetry of the pixel crosstalk in SPR measurements has not been explicitly considered. We find that the  $\alpha$  values for the top and bottom neighbors can swing from 0.03 all the way to 0.25 as a result of the column offset, depending on the biases applied and operating conditions.

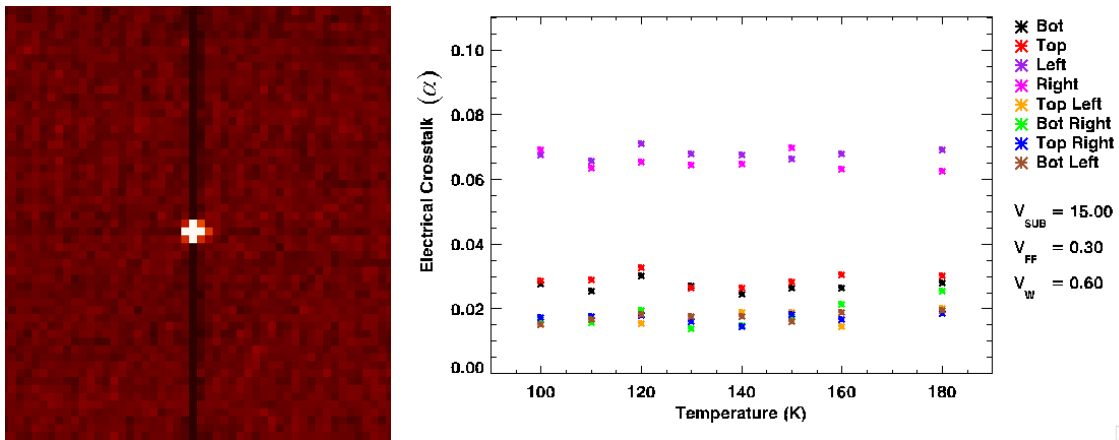


Figure 6.16: In SPR the coupling with the column neighbors is consistently lower than that for the row neighbors. The left image shows that the entire column of the pixel sees a slump in signal when  $V_{RstWin} = 1.0$  V and  $V_{RstFF} = 0.15$  V. A dark exposure in which the single pixel was not reset has been subtracted. For this case the column is about 11 mV below the rest of the array. The right plot shows that the top and bottom neighbors can have very low  $\alpha$  values in SPR.

**Front Surface Diffusion** Another unexpected finding is that for reset voltages above 0.8 V and temperatures above 150 K, a significant outward diffusion of charge occurs from the pixel under reset to the surrounding ones. The diffusion, shown in Figure 6.17, generates a rise in signal for pixels well beyond the nearest neighbors at temperatures above 160 K. The signal in these nearest pixels see a quasi-exponential rise with time. Further out, the pixels integrate at the rate expected from dark current and then begin to rise at the quasi-exponential rate when the diffused charge has reached them. The radius to which the carriers diffuse in a time  $t$  and the slope in the signal rise increases as  $V_{SUB}$  decreases. For temperatures below 140 K, the signals do not change significantly from their bias value.

The strong temperature and backside bias dependence of this diffusion suggests it is caused by thermionic emission of holes over the interpixel potential barrier. For temperatures above 140 K, we assume the hole current has the form

$$J_p = A_o * (T - T_{th})^2 e^{\frac{V_{RESET} - V_{th} - f(V_{SUB})}{kT}}, \quad (6.20)$$

where  $A_o$  is a constant,  $T_{th} \sim 140$  K is the threshold temperature below which the current is not detectable in the surrounding pixels and  $V_{th} \sim 0.8$  V is a threshold voltage which represents the barrier height between two neighboring pixels. From the limited data collected in the SPR experiment, the function  $f(V_{SUB})$  is not well determined. A closed analytical form may not exist since it depends on the potential profile between the back surface and the surface above the interpixel gap, which is inadequately treated without numerical integrations. However, it is clear that  $f(V_{SUB})$  is an increasing function of  $V_{SUB}$  since it effectively strengthens the barrier between the pixels. Invoking the continuity equation, the neighboring pixels will see an increase in signal if the hole

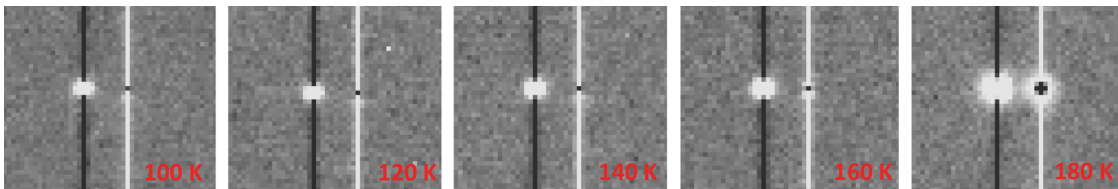


Figure 6.17: These images show charge diffusion and persistence in SPR at temperatures from 100-180 K. Each image is the product of subtracting the last read of an exposure where the pixel to the right was selected as a guide window and read 100 times between full frame reads (no resets applied) from the last read of an exposure where the pixel to the left was selected as a guide window and reset to  $V_{RstWin} = 1.6$  V 100 times between full frame reads. The former was taken approximately 45 seconds after the latter, so the signal in the pixel to the right is a form of persistence. At 160 K and above, the core-halo structure (see Section 7.2) around the pixel is evident. The colors in the linear stretch—white corresponds to +12.8 mV and black to -9.8 mV—are inverted for the core-halo structure since it has been subtracted from another exposure.

current in to the pixel,  $J_p^{in}$ , is greater than the hole current out of the pixel,  $J_p^{out}$ . This explains how some of the pixels initially see a rise in signal and then a decline in signal some time later.

Figures 6.18 and 6.19 further support the theory that a diffusive hole current is leaving the center pixel. These figures show the relationship between the programmed reset voltage of the single pixel and the ADU value at which it is measured during a full frame read. If carriers were not leaving the pixel, the data points at a given value of  $V_{RstWin}$  should all lie on top of each other.<sup>4</sup> But because of the diffusion, there is some dispersion. When less resets are applied to the single pixel (25, for instance), the amount of excess carriers that escape the pixel during the period where it is not being reset is sufficient to bring the signal down within range of the ADC. When more resets are applied, there is an ample supply of excess carriers to keep the ADC railed despite the diffusion. The anomalous data point at  $V_{RESET} = 1.6$  V and  $T = 100$  K is a result of the dewar warming up during testing.

Although the effect this diffusion has in SPR tests is quite dramatic, the role it will play in astronomical applications may very well be insignificant. The pixel under reset is very near saturation before the leakage takes place. If a star is bright enough to saturate pixels at its center, doing photometry or astrometry on it will be fruitless regardless of whether or not there is a diffusion of holes to the surrounding pixels. And if it is a medium brightness star, the pixel ramps can be examined only for the time span before the saturation takes place to obtain the photocurrent. Also, the SPR experiments described consisted only of tests up to  $V_{SUB} = 25$  V. It is possible that increasing  $V_{SUB}$  to a higher value could diminish the effect further. More experiments need to be done to confirm this.

Lastly, it should be noted that controlling the inter-pixel barrier height can be effectively accomplished through the use of gates placed in between the indium bump bonds. The voltage on the gate can be changed to increase or decrease the barrier, by accumulating or inverting the front surface of the detector, respectively. In the RVS SiPIN detectors, the gate is typically set at 5 V, which should result in a substantial decrease in the inter-pixel diffusion [38].

---

<sup>4</sup>Note that the disparity between the 100-130 K and 140-180 K ranges is due to the unexplained offset mentioned in Section 4.3.7.1.

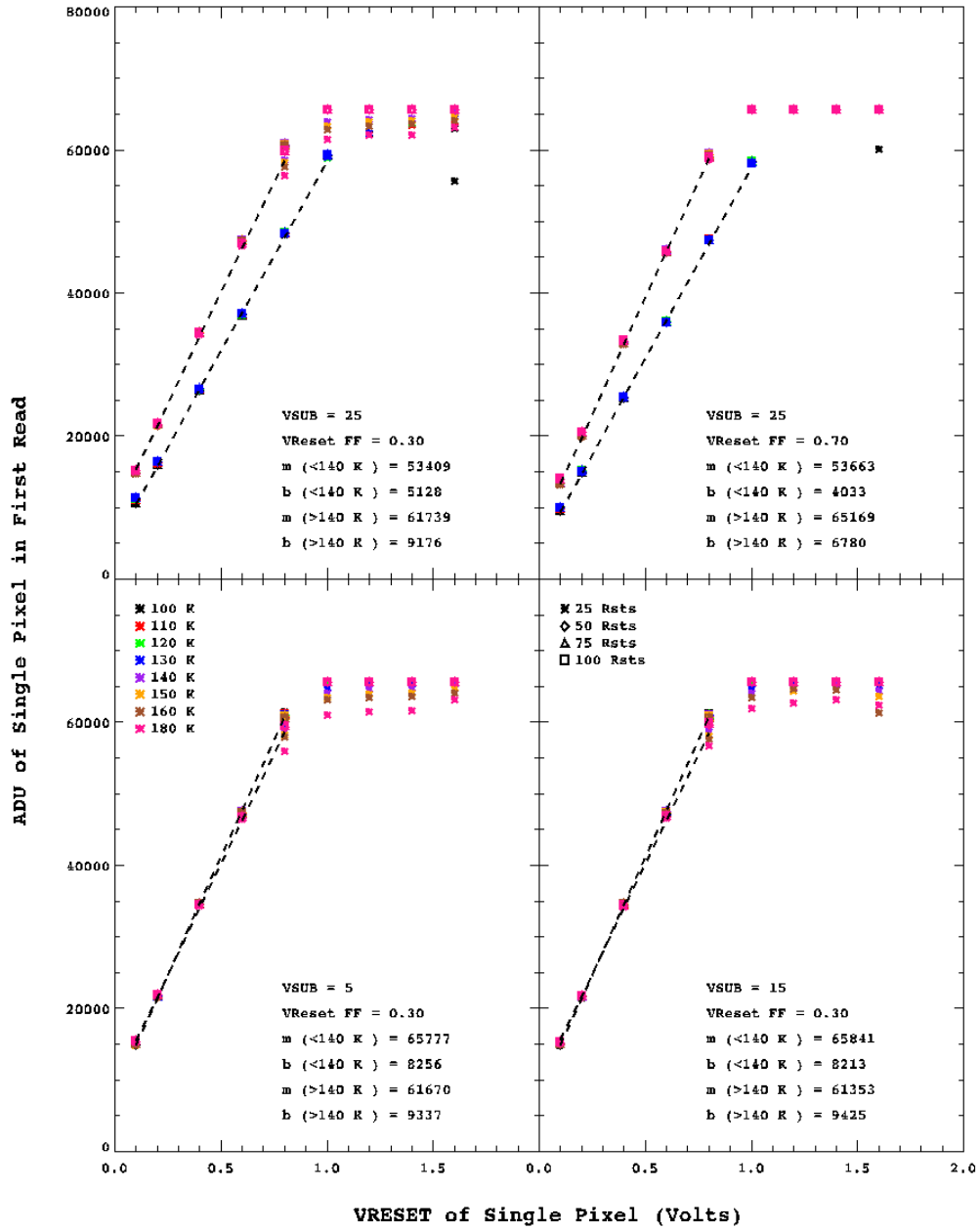


Figure 6.18: The output signal in ADU vs. the value of VRESET applied for a single pixel subject to single pixel reset in guide mode. Four cases with different values of VSUB and VRESET for the full array are shown. The legend shows the different temperatures as different colors and the different symbol shapes indicate the number of resets applied to the single pixel between full frame reads of the array. The dashed lines show the fitted slope,  $m$ , and intercept,  $b$  in terms of ADU/Volts. These numbers are also indicated in the diagram.

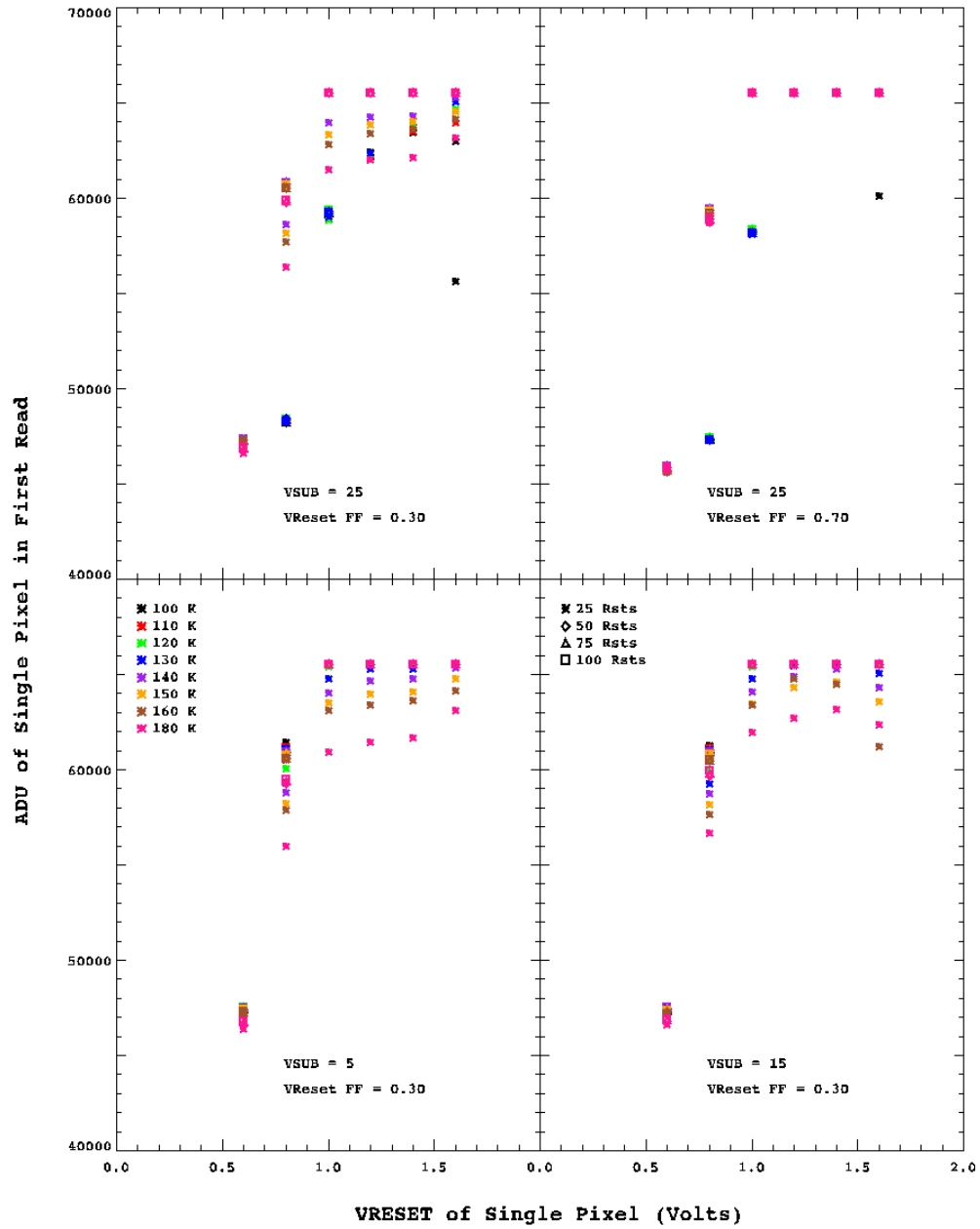


Figure 6.19: The same plots as in Figure 6.18 with only a small region shown for high values of VRESET. The legend shows the different temperatures as different colors and the different symbol shapes indicate the number of resets applied to the single pixel between full frame reads of the array.

## 6.2 Electronic Crosstalk

Electronic crosstalk can occur in several different ways in HyViSI detectors and hybrid detectors in general. Pixels may couple to supply buses. They may also couple to the other pixels in their respective column. And if multiple outputs are used, the signals from the pixels that are simultaneously selected can affect one another. Each of the last two cases will be examined in turn. For a good discussion of supply bus coupling, see Moore [24].

### 6.2.1 Column Bleeding

In many of the astronomical exposures recorded with the HyViSIs, a bleeding of signal is observed in the columns above pixels saturated by bright stars. Figure 6.20 shows the effect in a very pronounced form, as this is a mosaic where the same bright star saturated pixels in all of the individual exposures and the read noise has been beaten down after slope fitting the pixels and taking the mean. The

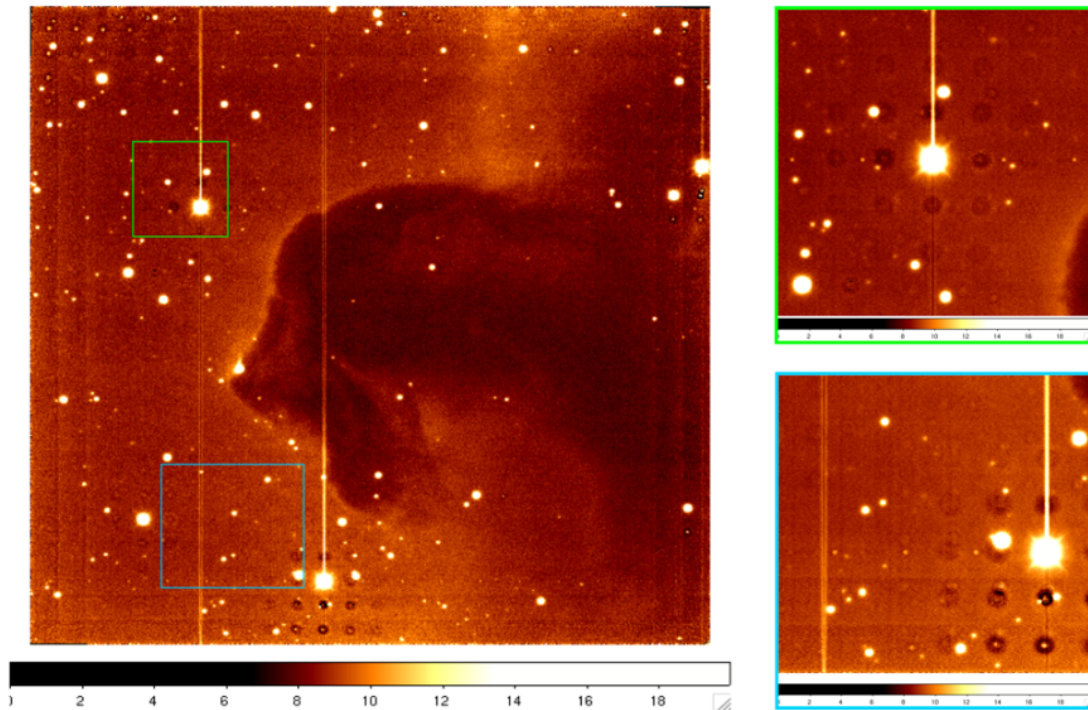


Figure 6.20: If a pixel has sufficiently high voltage, it will bleed into its column for a certain amount of time after it is selected. This is a mosaic of the Horsehead Nebula that shows the effect. The dark region in the center columns above the bright stars occurs because the image that went into the mosaic were *slopefits* with pixel values that represent the change in voltage with respect to time. The raw images show elevated voltages for all the pixels in the region. The black circles are due to persistence effects that will be described in the next chapter.

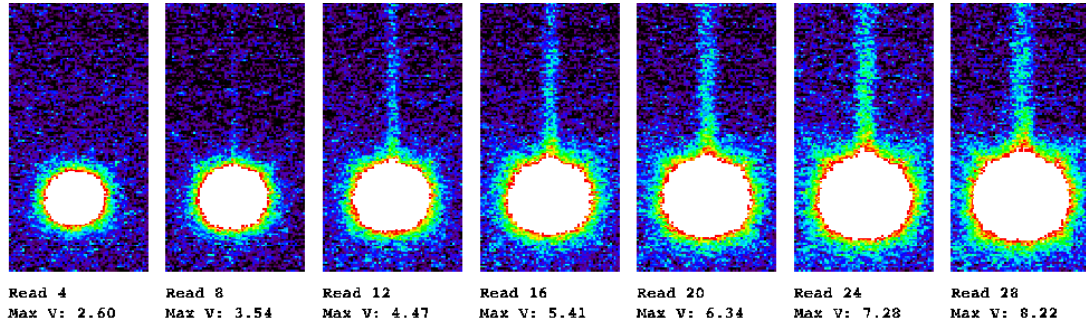


Figure 6.21: The column crosstalk does not depend on the instantaneous photocurrent, but rather occurs after a certain threshold voltage. Each image is a snippet from a 30 read exposure of a star that produces  $15,000 \text{ e}^-/\text{s}$  in the center pixel. The sky value has been subtracted and the min/max of the scale are  $-10/100 \text{ ADU}$ . The raw voltage in the pixel, listed at the bottom of the snippet, is just an extrapolation from the SIDECAR conversion of ADU to  $\mu\text{V}$  from Equation 3.11. Although inaccurate for values above 3.5 volts or so, this shows the onset of the column bleeding when the pixel nears 3.3 Volts.

same bleeding effect is also observed for the dark current *volcanoes* described in Section 4.2.4.

As evidenced by the readout sequence in Figure 6.20, the effect is not initiated until the pixel has reached a voltage of about 3.3 volts.<sup>5</sup> This voltage is not arbitrary. It corresponds to the digital ( $V_{DD}$ ) and analog supply ( $V_{DDA}$ ) voltages as well as the source node voltage for the internal current source of the pixel source followers,  $V_{BIASPOWER}$ . If the voltage at the  $\text{p}^+$  integrating node rises above this, the source of the unit cell FET can no longer follow the gate.

After the threshold has been reached by a particular pixel at  $i, j$  the pixels in the columns immediately above it ( $j+1, j+2, \dots, j+\Delta j$ ) experience an offset in signal of about +3-6 millivolts. The strength of the offset decays with an exponential signature as a function of  $\Delta j$ , i.e.

$$S(i, j + \Delta j)_{\text{after offset}} \sim S(i, j + \Delta j)_{\text{before offset}} + 4.5 \text{ mV} * \exp(-\Delta j/J), \quad (6.21)$$

where  $J$  is 50 pixels or so. If the saturated pixel is near the top of the detector, the decay will wrap around to the bottom of the detector. This increase is a constant offset to the signal that does not get larger with time; the affected pixels continue to integrate at their previous rate after it has occurred.

<sup>5</sup>Although there is no lack of data that shows the effect, the detector output becomes nonlinear at about  $V = 3.0 \text{ V}$ . The exact onset voltage of the nonlinearity depends on the temperature and  $V_{BIASGATE}$ . Thus, 3.3 V is an estimate.

### 6.2.1.1 Explanations and Mitigation

The behavior described rules out the possibility that the column bleeding occurs in the silicon detector layer. It is not unreasonable to guess that saturated charge carriers might bloom preferentially along the columns in the detector, but there is no way they would wrap around from the very top row to the very bottom row. And if it was somehow an artifact of the control electronics, we should expect the response to be identical along the rows. It must therefore be generated in the multiplexer.

Pixels in the same column share a common vertical read bus in the multiplexer, A.K.A. the column bus. When a given row is selected, all of the pixels in that row are connected to their respective column buses through the CMOS *row select switch*. When a given pixel is selected, its column bus is connected to the horizontal read bus through another CMOS switch, the *column select switch*, and the column bus then carries an electrical current to the output. If there is sufficient capacitance between the input and output of the row select switch, then it is possible that a transient voltage will be present at the output after it has been closed and the next row has been selected. Once the column bus is again selected for the subsequent row, the transient voltage may couple to it and cause an offset in the signal. Unfortunately, the details of the multiplexer are not available for study to pinpoint the exact location of this stray capacitance.

While this effect is observed in all of the H1RG and H2RG devices tested, it is not observed in the H4RG. The reason for this is that the H4RG pixel has an anti-blooming diode (in parallel with the photodiode) that clamps the gate voltage at  $V_{DDA}$ , preventing the threshold voltage from being reached. Also, the effect appears to subside at lower values of  $V_{BIASGATE}$ . It is present in all of the data recorded with the SIDECAR, which operated with  $V_{BIASGATE} = 2.29$  V. However, it is not present in any of the data recorded with the ARC electronics, which had  $V_{BIASGATE} = 1.90$  V. In the latter case, though, strong bleeding along the rows occurred instead. A dependence on  $V_{BIASGATE}$  should be expected since this is the voltage that governs the amount of current flowing through the buses and to the pixel drain. However, a quantitative relationship has not been established. A future experiment should be undertaken in which the bleeding of saturated pixels or the dark current volcanoes (which can be done in the dark) is observed as a function of  $V_{BIASGATE}$ ,  $V_{DDA}$ , and  $V_{BIASPOWER}$  to better understand the effect and how to prevent it from occurring.

### 6.2.2 Output Coupling

Another type of electrical coupling that occurs in the HxRG multiplexers is inter-channel, or output, coupling. When  $N$  outputs of the detector are being used,  $N$  pixels in a given row are being selected concurrently. If one of these  $N$  pixels is transmitting a large signal to its output, the other  $N - 1$  pixels may see an elevated signal, or *ghost*. An example of this is shown in Figure 6.22. The location of the ghosts will depend on the location of the saturated or near saturated pixel with respect to the outer edges of the channel as well as the read direction in each channel.

For the data taken with H2RG-32-147 and H1RG-022 at the Kitt Peak telescope the ghost signal appeared solely as a positive offset. However, for data recorded with H2RG-001, negative offsets were also observed, indicating two distinct types of behavior. Finger et al. observed the latter type in a HgCdTe H2RG [100]. As was done in their studies, the control electronics have been tested separately and eliminated as a possible source of the channel coupling. The mechanism that generates the ghosts in the HgCdTe devices is believed to be the same as that for the HyViSI. The primary difference in the purely positive coupling and positive/negative coupling is believed to due to the use/absence of the output source follower in the signal path.

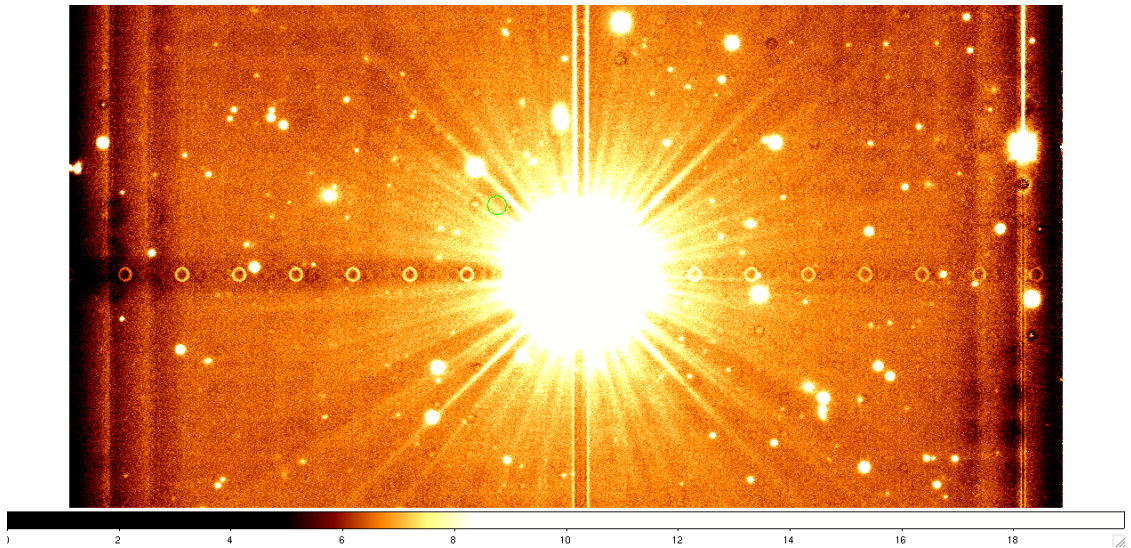


Figure 6.22: Saturated stars show up as ghost images in the other channels of the multiplexer. This is a mosaic of *slopefit* images of the bright star SAO 117637. The donut shape with the bright annulus and dark core is due to the slope fit. In a raw image, all pixels in the ghost show up with a positive offset. Also, in a raw image all 32 channels show a ghost image. The mean filtering of the mosaic removed some of the ghosts, but not all of them.

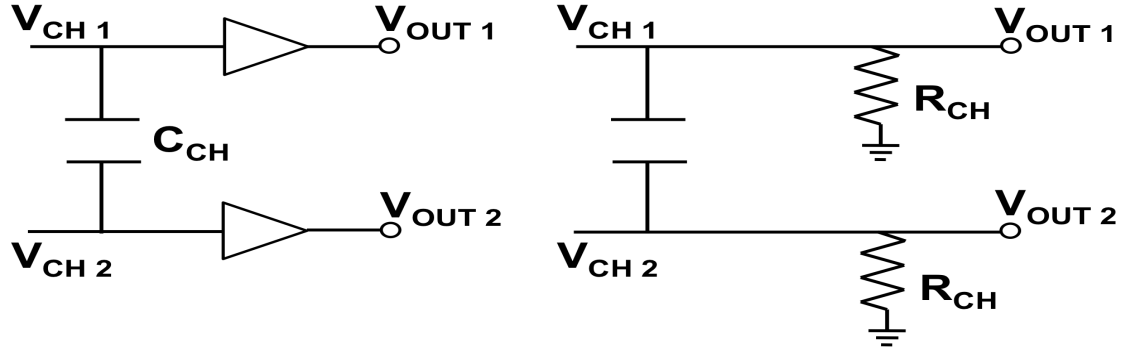


Figure 6.23: Circuit diagrams to explain output coupling through inter-channel capacitance. (Left) For the case where the output source follower is used, only positive signal coupling is observed, suggesting displacement current through a coupling capacitance. (Right) For the case where the output source follower is not used, the ghost signal has sign corresponding to the derivative of the signal in the offending pixels, suggesting an RC differentiator.

### 6.2.2.1 Coupling with Output Source Follower

With the output buffer placed in the signal path for each channel, the signal from the pixel sees a very high impedance. If a coupling capacitance exists between the buses, a displacement current,  $i_{dis}$ , between them may be responsible for the signal in one channel showing up in the others. No quantitative or qualitative information on the architecture of the channel routing is available (e.g. the pitch of the wires or their orientation). But a simple two channel model like the one on the left in Figure 6.23 may be used to express the voltage change on an affected output as  $dV_{OUT\ 2}/dt = i_{dis}/C_{CH}$ , where CH 1 is the line that carries the high voltage level. Instead of attempting to calculate  $i_{dis}$  and  $C_{CH}$ , a coupling constant,  $\alpha$ , is used to relate the voltage changes:

$$\Delta V_{OUT\ 2} = \alpha \Delta V_{OUT\ 1}. \quad (6.22)$$

The average measured value is  $\alpha = 3.5 \times 10^{-3}$ , an extremely small coupling. Thus, the output coupling with the source follower enabled only presents itself for signals near full well or after multiple reads have been averaged to reduce the read noise.

The coupling grows even weaker as the channel separation grows. Note the rings to the very right in Figure 6.22 are substantially fainter than the ones closest to the star. It should be noted that the current source supplied to the output buffer by the SIDECAR and ARC electronics may play a part in the coupling. While coupling of the amplifier channels on these boards were tested by providing an input voltage from a power supply, the extremely low output impedance of the supply placed little or no demand on the current sources in these tests. A higher impedance source should be used to check for channel coupling in the electronics.

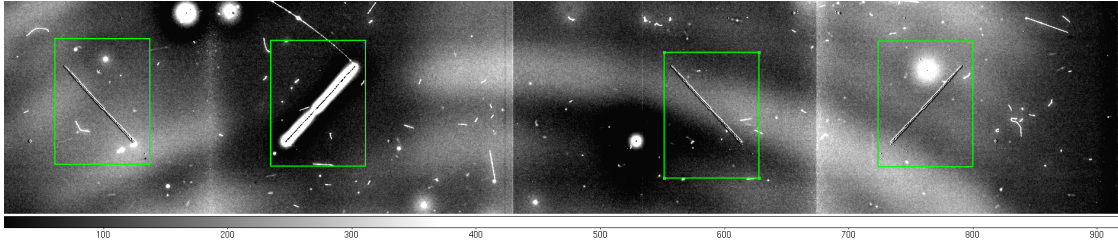


Figure 6.24: A last read minus first read image taken from a 100 read exposure with H2RG-001 operating in 4 output mode. The read direction in the channels is represented as  $\leftarrow\rightarrow\leftarrow\rightarrow$ . A scratch in the detector creates high leakage current for the large region shown in the second green box to the right. In the other green boxes the ghost images show positive coupling while the voltage on the second output increases during the clocking sequence and negative coupling when the voltage is decreasing.

### 6.2.2.2 Coupling without Output Source Follower

The output source follower was disabled for noise tests performed on H2RG-001. These data show a negative coupling as well as a positive one. Figure 6.24 shows an example where a high leakage current area in H2RG-001 (read out through output 2) couples to the other 3 outputs being used. The read directions for the channels are  $\leftarrow\rightarrow\leftarrow\rightarrow$ . As can be seen in the figure, if the signal in channel 2 is increasing during the clocking sequence, the signals in the other outputs couples positively. And if it is decreasing during the clocking sequence, it couples negatively

As Finger et al. note, this is the behavior exhibited in a simple RC differentiator circuit [100]. Such a circuit is shown in the right of Figure 6.23, with  $C_{CH}$  representing the coupling capacitance and  $R_{CH}$  representing some resistance to ground.  $R_{CH}$  might be present in the multiplexer itself or at the preamplifier stage. Every time a new pixel is selected, the signals at the output swing by  $\Delta V_{OUT}$  from the previous pixel voltage to a new pixel voltage. If  $CH$  1 is carrying the high voltage, then the expected change in voltage on  $CH$  2 will be:

$$\Delta V_{OUT\ 2} = R_{CH}C_{CH} \frac{\Delta V_{OUT\ 1}}{\Delta t} \quad (6.23)$$

where  $\Delta t$  is some fraction of the sampling time for a given pixel. Finger et al. show that the coupling indeed worsens when the pixel time is shortened [100] and measure a coupling of about 0.001 at a pixel time of 10  $\mu\text{s}$  in a HgCdTe H2RG. In HyViSI H2RG-001, we measure a coupling in the range 0.0005-0.0018 (0.05%-0.18%) with a pixel time of 10  $\mu\text{s}$  and  $V_{BIASGATE} = 2.05$  V.

The coupling without the output source follower diminishes when  $V_{BIASGATE}$  is decreased. This makes sense as the increased drain to source current of the pixel source follower decreases the settling time for each output. Of course, for applications that do not require fast full frame readout, one may operate the sensor with only one output to avoid this effect altogether.